Concave Bump for Impinging-Shock Control in Supersonic Flows

Erich Schülein,* Christian Schnepf,† and Sebastian Weiss‡

German Aerospace Center DLR, Institute of Aerodynamics and Flow Technology, Göttingen, 37073, Germany

In the present study, a novel concave bump for impinging-shock control in two-dimensional supersonic flows is investigated. An analytical method for preliminary bump design based on a generalized shape of a shock-canceling bump has been developed and verified numerically. An extensive proof-of-concept study was performed at a freestream Mach number ranging from 2.5 to 5.0 for shock-generator angles varying from 6 to 12 degrees. It could be demonstrated that a concave bump designed for a given flow-deflection angle is capable of significantly reducing the size of the separation bubble as well as the total pressure losses throughout the Mach number range investigated. The achievable gains depend on the Mach number, the flow-deflection angle, and the relative impingement position of the incident shock front on the bump. The highest values of separation-length reduction (up to 100%), momentum thickness reduction (up to 31%), and pressure recovery factor increase (up to 33%) were obtained at the optimum shock impingement position for the largest deflection angle studied. The concave bump is less effective, and in some cases even disadvantageous, when the incident shock wave does not optimally strike the bump crest.

Nomenclature

c_f	=	skin-friction coefficient
c_p	=	pressure coefficient
L	=	half-length of the concave bump
L_{sep}	=	separation bubble length
L_1	=	length of the rounded part of the concave bump
M	=	Mach number
p	=	pressure
$p_A,$ p_B	=	pressure detected at taps upstream/downstream of the crest
$p_{0,y}$	=	wall-normal total pressure profile
$\bar{p}_{0,y}$	=	total pressure averaged within a near-wall layer of 8 mm
R	=	reattachment point
R_1	=	radius of the rounded part of the concave bump
Re_{unit}	=	unit Reynolds number per 1 m length
S	=	separation point
T	=	temperature
ϵ	=	impinging-shock angle
u, v	=	longitudinal and vertical velocity components
x, y	=	longitudinal and vertical coordinates
β	=	shock-generator deflection angle
Δp_{BA}	=	pressure difference, $p_B - p_A$
δ	=	boundary-layer thickness, $U_\delta = 0.99U_e$
δ^{**}	=	boundary-layer momentum thickness
γ	=	heat capacity ratio
θ	=	local flow/bump-contour deflection angle
ρ	=	density

Subscripts

cr	=	bump crest value
e	=	conditions outside the boundary layer
imp	=	impingement point value
in	=	local incoming flow conditions
max	=	maximum value
min	=	minimum value
nom	=	nominal (design) flow conditions
opt	=	optimum value
R	=	reattachment point value
ref	=	reference flow conditions (without bump)
S	=	separation point value
w	=	wall conditions
δ	=	conditions at the boundary-layer edge
0	=	total flow conditions
1	=	undisturbed flow conditions upstream of the interaction
2	=	flow conditions behind the impinging shock (nonviscous)
3	=	flow conditions behind the reflected shock (nonviscous)
∞	=	freestream flow conditions

I. Introduction

SHOCK-WAVE/BOUNDARY-LAYER interaction (SWBLI) is known to be one of the key physical phenomena with regard to performance and starting limits of supersonic/hypersonic inlets [1–3]. In the inlets with internal supersonic compression, a series of successive SWBLI events typically develops. The strongest interaction in this series, which occurs in the entrance area due to the influence of the cowl shock on the boundary layer, dominates the flow. The influence of flow distortions and total-pressure losses caused by this initial interaction is far-reaching for all subsequent interaction events and, finally, for the inlet performance itself. Therefore, the control of the cowl-shock-induced SWBLI is a principal topic of each inlet design.

Figure 1 schematically shows an inlet with mixed compression (1—compression ramp; 2—inlet cowl), in which the supersonic flow is compressed in several oblique shocks, external (3) and internal (4, 5), before it is slowed down to subsonic speed by the terminal shock (6). The pictures illustrate some existing solutions for controlling the cowl-shock interaction and preventing flow separation. The most popular and effective of these is to bleed the boundary layer from the interaction zone to the outside (Fig. 1a; 7—bleed air plenum chamber). This significantly increases the robustness of the flow with regard to adverse pressure gradients (see, e.g., [4,5]). However, bleeding off some of the duct flow inevitably increases nacelle drag and decreases mass flow through the combustion chamber, each of
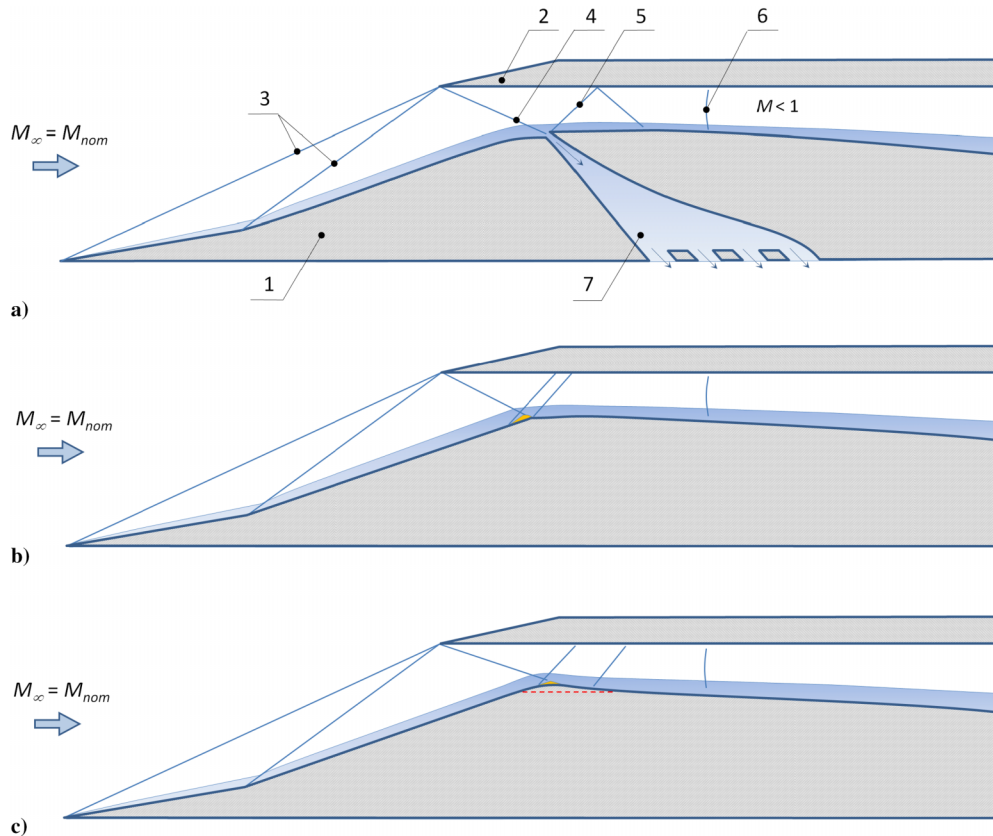
Fig. 1 Simplified sketches of a supersonic (ramjet) inlet at the nominal (design) freestream Mach number $M_\infty = M_{nom}$: a) equipped with a boundary-layer bleed system; b) configured with a reflected-shock-cancellation kink at the duct wall; c) designed with a 2-D bump integrated at the cowl-shock-impingement location. Yellow regions indicate flow-separation bubbles.

which affects the overall performance of the propulsion system [4]. When flying in the range of higher supersonic Mach numbers, a further problem arises, which completely questions the use of a bleed system for the air-breathing hypersonic vehicle. This is the enormous additional heat load on the structure, which requires special thermal protection measures along the entire exhaust duct/plenum chamber (7, Fig. 1a).

A rather simple but elegant way to prevent losses induced by shock waves is the use of the so-called beneficial interference in the design of inlet channels (Fig. 1b). It is inspired by the well-known Busemann biplane concept (see, e.g., [6], p. 116). The reflected shock can be completely eliminated by aligning the wall, downstream of the impingement point, parallel to the nominal flow direction behind the impinging shock wave. Of course, the resulting compression effect of such an adjusted flowpath is throttled and roughly only half as strong. However, if a kink in the channel path is required anyway for configuration reasons, local contour adaptation can be very advantageous. It is important to note that the effectiveness of such a solution depends on the hitting accuracy of the incident shock front and thus has a relatively high sensitivity to the variations of the inflow Mach number.

The application of a contoured shock-control bump at the cowl-shock-impingement location directly behind the expansion kink (Fig. 1c) seems to be able not only to improve the robustness of the inlet but also to extend the Mach number range permissible for a given channel geometry (see, e.g., [7,8]). Shock-control bumps of this kind are well-known from earlier transonic-wing-related shock-control investigations (see, e.g., [9–13]). The task of the bump is here to split a strong single shock wave into a multiple-shock system, which is favorable with regard to wave drag and flow separation. Of course, except for contoured bumps, all other shock-control methods acting in a similar way (passive ventilation through porous walls, slots or grooves [12,14]) could be alternatively applied for the cowl-shock control in accordance with the concept sketched in Fig. 1c.

Regardless of the shock-control method, it must be adapted and optimized to given parameters to achieve a considerable shock-control effect, both as a single device and as a part of the entire inlet as well. Given the amount of parameters involved, this is a challenging task. The improvement potential of a single-device optimization was clearly demonstrated recently by Shinde et al. [15], studying numerically the control of transitional SWBLI on a flat plate by surface morphing in the interaction area. Two different strategies of adaptive surface morphing were studied using direct numerical simulations to find the optimal local surface deformation at a constant Mach number of 2. In the first approach, the controlled zone of the surface was deformed to find the optimal height of a conventional bell-shaped shock-control bump. The second strategy was to find an arbitrary contour, which enables an attached flow throughout the entire interaction zone and prevents the occurrence of laminar-turbulent transition. The latter optimization strategy was clearly more demanding but led to success with regard to the assigned separation-control objectives. Furthermore, it reveals, by the way, a new noteworthy shape of the contoured bump, which differs from the conventional bell-shaped one. This new contour has a characteristic concave shape marked by an expansion kink directly at the peak. Hereinafter, this contour is referred to as *concave bump*.

In the latest study by the same authors [16], new high-fidelity large eddy simulations were used to investigate surface morphing as a possibility to reduce the size of separation bubbles in turbulent flows at a Mach number of 2.7. Unlike in the previous study, the control surface was only allowed to deform within feasibility constraints based on material properties. The leading and trailing edges of the control surface were clamped so that only a wavelike contour could be realized. Unfortunately, the contour optimized within the bounds fell far short of the success described for the concave bump, since the separation bubble could not be completely eliminated but only reduced in size by about 50%.

One of the most important findings of the former work [15] is the remarkable wall-pressure distribution observed with the optimized bump contour. This specific pressure distribution, which can best be described by the shape of a rounded ramp, seems to prevent the separation of the flow. Our interpretation of the concave-bump effect on the surface pressure distribution and on the SWBLI observed in [15] is sketched in Fig. 2. The resulting wall-pressure distribution appears to be determined almost entirely by the shape of the concave bump, with no appreciable effects from viscous–inviscid interactions. The softly curved bump surface upstream and downstream of the expansion kink, complemented by the reflected-shock cancellation at the expansion kink, induces a gradual (isentropic) flow compression along the wall. Thus, in consequence, it offers itself to use in the preliminary design phase some simplified gas-dynamic relations instead of the time-consuming high-fidelity optimization methods mentioned previously.

The aim of the present work was to develop and to verify a simplified method for preliminary concave-bump design, which is based on a generalized representation of the shock-canceling bump shape. The idea was that the particularly favorable pressure distribution at the model surface can be produced simply by shaping the wall contour in the SWBLI zone. For this reason, an analytical study was first performed to obtain the appropriate bump contour for a supersonic inviscid flow with an incident oblique shock wave. It was found that the normalized deflection angle of the bump surface can be represented uniformly as a function of the normalized longitudinal coordinate. The respective normalization parameters here are the flow-deflection angle of the incident shock wave and half the length of the concave bump.

Following the analytical study, the potential of the novel bump design was investigated numerically and experimentally for a wide range of Mach numbers and shock-wave intensities. For this purpose, a canonical two-dimensional (2-D) impinging/reflected shock interaction case, well-known from different fundamental studies on SWBLI [13,17], was used as a test configuration. For each of the four discrete flow-deflection angles nominally selected for this study,

a specific bump contour was analytically determined using the design procedure presented in Sec. III.A. In the main part of the study, for each combination of Mach number and shock-generator angle, the shock-impingement point at the respective bump was varied stepwise and systematically over the entire length of the bump. In this way, the most effective shock-impingement point could be selected as the so-called design position from a large number of predominantly off-design shock-impingement points. The shock-generator angle β nominally corresponded to the maximum deflection angle θ_{max} in each case. The influence of the local deflection angle of the flow, which would also be very relevant for practical applications, was not explicitly studied here and therefore kept for the future.

II. Test Conditions, Test Model, and Numerical Setup
A. Wind Tunnel

The experimental part of investigations was conducted in the Ludwieg tube facility RWG at DLR Göttingen (Fig. 3). This facility covers a Mach number range of $2 \leq M_\infty \leq 7$ and an unit Reynolds number range of 2×10^6 m$^{-1} \leq Re_{1,\infty} \leq 11 \times 10^7$ m^{-1} (see Table 1). The specific feature of a Ludwieg tube is the usage of a long expansion tube as pressure reservoir, which is closed at one end and has a gate valve attached to the other end, followed by a supersonic nozzle, test section, and dump tank. After opening the gate valve, the airflow is started by expansion waves that travel to the closed tube end, are reflected there, and travel back. As long as these waves do not reach the nozzle throat, test gas flows out at nearly constant stagnation conditions through the nozzle and the test section into the dump tank. The Ludwieg tube RWG has two interchangeable storage tubes, the unheated tube A and the heated tube B, each with a length of 80 m, resulting in a run time of about 300–350 ms. The low operating costs, a relatively large test section, and sufficiently good optical accessibility make this facility ideally suited for systematic basic parameter studies and the predominant use of optical experimental techniques.
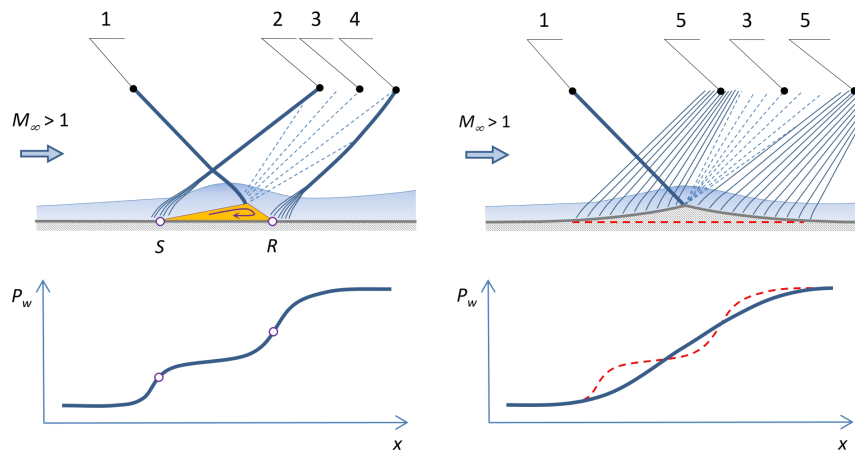

Fig. 2 Flow topology and wall-pressure distribution: left) uncontrolled baseline case and right) concave-bump case. 1—impinging shock; 2—separation (reflected) shock; 3—expansion waves; 4—recompression shock; 5—compression waves; R—reattachment point; S—separation point; and dashed red line—baseline shape.
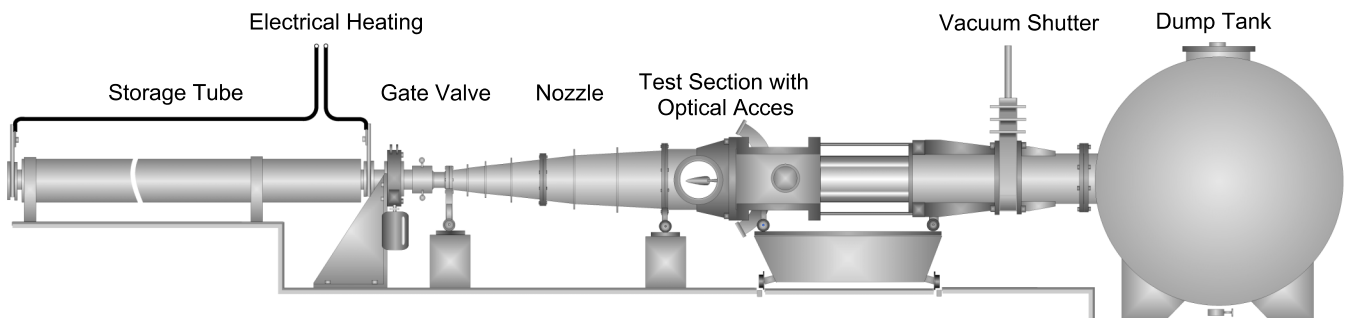

Fig. 3 Sketch of the Ludwieg tube facility RWG at DLR Göttingen.

Table 1   Ludwieg tube flow-parameter range

Tube	A	A	A	B	B	B
Mach	2	3	4	5	6	6.85
p_0, MPa	0.05–0.7	0.06–0.6	0.08–1.0	0.4–2.9	0.4–3.4	0.4–3.6
T_0, K	236–262	241–267	258–287	340–610	410–640	440–655
$Re_{\text{unit},1}$, 10^6 m^{-1}	10–110	6–70	4–60	5–55	3–28	2–17
Test section	0.34×0.35 m^2	0.5×0.5 m^2	0.5×0.5 m^2	$\varnothing 0.5$ m	$\varnothing 0.5$ m	$\varnothing 0.5$ m

B. Test Model and Test Conditions

A sketch of the investigated wind-tunnel model is shown in Fig. 4a. The base configuration consists of a shock-generator wedge positioned above the main flat plate. Both the flat plate and the shock generator can be moved and replaced independently of each other. In addition to the usual baseline flat plate, four further plate models each equipped with a 2-D concave bump were used. All these plates have

sharp leading edges (leading-edge radius in the order of 10 μm) and are trapezoidal in top view. Each of them has a length of 353 mm and a width of 300 mm at the leading edge and 180 mm at the trailing edge. The bump length in flow direction and the distance between the flat-plate leading edge and the bump crest were nominally kept constant and equal to correspondingly 60 and 280 mm. Each bump contour investigated was specifically designed for a given shock-generator
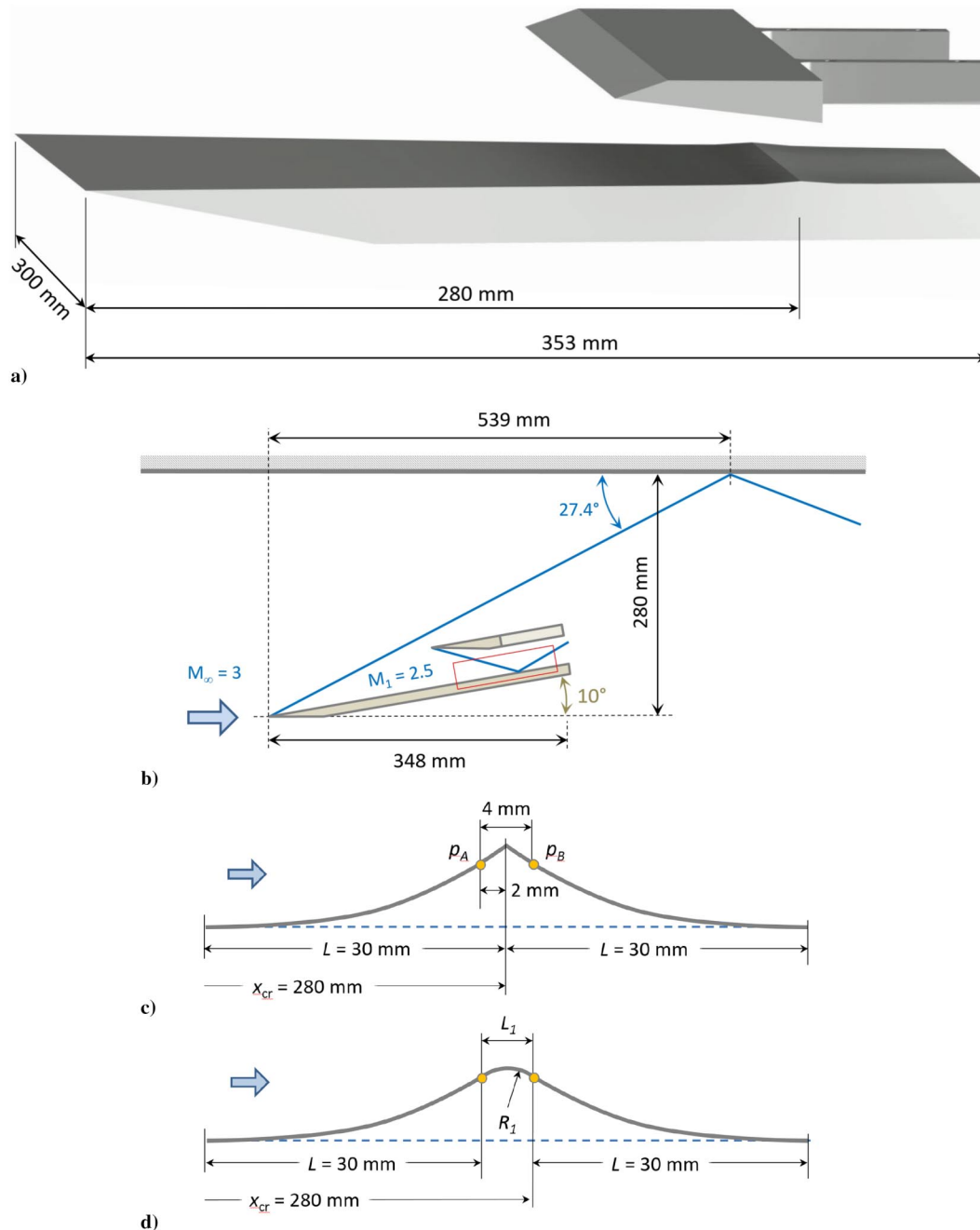
a)

b)

c)

d)

Fig. 4   Sketches of the: a) test model with a concave bump and shock generator, b) specific model setup realized to achieve $M_1 = 2.5$, c) bump contour with pressure taps studied experimentally, and d) configuration to study the influence of bump-contour rounding instead of a sharp-edged kink.

angle β, and each flat-plate model with a bump was only tested with the appropriate shock-generator wedge. Four different shock generators with flow-deflection angles β of 6, 8, 10, and 12 deg were investigated. All shock generators were 80 mm in length and 200 mm in width. The vertical distance between the flat-plate surface and the leading edge of the shock generator was variable, enabling an independent fine adjustment and variation of the shock impingement location. In this work, the shock-impingement point x_{imp} is defined as the virtual intersection of the undisturbed shock front with the x axis of the flat plate. To determine this cross point in the experiment, the detected path of the undisturbed shock front in the shadowgrams was linearly extrapolated to the virtual x axis.

Each wind-tunnel model equipped with a bump was also provided with two separate pressure taps, one on the windward side (p_A, see Fig. 4c) and one on the leeward side of the bump (p_B), which were connected to fast-response pressure transducers of the type Kulite® XT-190M-1BAR-A. The longitudinal distance between these taps and the crest was 2 mm each. Transducer signals were acquired at a sampling rate of 5 kHz using an Endevco® model 136 DC amplifier. The rated accuracy of pressure transducers is quoted by the manufacturer as $\pm0.1\%$ of full scale value ($\pm0.001 \times 10^5$ Pa = ±100 Pa). Its in situ calibration was made by varying the static pressure in the wind-tunnel test section before each run. For this purpose, the calibration pressure was detected additionally by a high-precision manometer.

The flow conditions investigated experimentally are presented in Table 2. As can be seen, the unit Reynolds number $Re_{\text{unit},1}$ was kept constant throughout the study, and three different Mach numbers M_1 were examined experimentally: $M_1 = 2.5$, 3.0, and 5.0. The interest in investigating more exactly the effectiveness of shock-control measures at lower Mach numbers is based on the known increase in interaction size and strength when reducing the upstream Mach number at fixed flow-deflection angles (see, e.g., [18,19]). The given values for Mach number M_1 and unit Reynolds number $Re_{\text{unit},1}$ correspond to the incident flow parameters above the main plate and ensure that a turbulent boundary layer is present upstream of the incident shock wave in each case. The pivoting suspension of the experimental model in the wind-tunnel test section allowed a variation of the Mach number M_1 upstream of the shock-generator plate by changing the inclination angle of the entire model as shown in Fig. 4b. With this trick, conditions $M_1 = 2.5$ were achieved with a freestream Mach number M_∞ of 3.0 and the test model inclination angle of 10 degrees. The sketch in Fig. 4b shows schematically the realized model setup including the nonviscous reflection of the induced shock wave at the upper wind-tunnel wall. The region of interest above the flat plate is indicated by a red frame.

C. Numerical Setup and Test Conditions

The DLR in-house flow solver TAU [20] was used for the numerical simulations in this study. TAU is a cell vertex hybrid structured/unstructured finite-volume flow solver based on the compressible Reynolds-averaged Navier–Stokes-equations (RANS). TAU can be used both for steady-state (RANS) and time-accurate (unsteady RANS) simulations. The Advection Upwind Splitting Method uniting flux-Difference and flux-Vector schemes (AUSMDV) was applied to achieve second order of spatial discretization in this study. The boundary layer on the flat plate was assumed to be fully turbulent.

In order to select the appropriate turbulence model and grid size, corresponding studies were carried out at the beginning of the work. First, 2-D simulations were performed on three different grids (coarse, medium, and fine) without varying the turbulence model (explicit algebraic Reynolds stress model) in the form of a usual grid study. In

Table 2   Summarized flow conditions at RWG experiments

M_1	$Re_{\text{unit},1}$, 10^6 m^{-1}	p_0, MPa	T_0, K	p_1, Pa
2.5	25.62	0.2312	269.8	13,533
3.0	25.58	0.2917	266.3	7,941
5.0	25.24	1.5679	425.6	2,964

this study, the coarse grid had about 310,000 nodes, the medium grid $\approx480,000$ nodes, and the fine grid $\approx1,100,000$ nodes. In the next step, the Reynolds stresses were modeled using the fine grid alternatively by the Spalart–Allmaras one-equation eddy viscosity model (SA), the Reynolds stress model (RSM), the Menter shear stress transport $k - \omega$ turbulence model (SST), and the aforementioned explicit algebraic Reynolds stress model (EARSM) from Hellsten. Results of these studies are shown for a single test case with $M_1 = 3$ at $\beta = 12$ deg in Tables 3 and 4 as the predicted positions of the separation and reattachment points x_S and x_R and as the length of the separation bubble $L_{\text{sep}} = x_R - x_S$. Additionally, the data are also presented as length ratios (in percent) to see the relations at a glance. All these results are shown separately for the reference situation (without bump) and with a flow control by means of the concave bump under investigation. For this comparison, a shock impingement location of $x_{\text{imp}} = 285.6$ mm was chosen, which deviated somewhat from the optimal location $x_{\text{imp,opt}}$ in the case with the bump (cf. Table 5) in order to deliberately obtain a reduced separation bubble as a second test case. Based on the results obtained, the EARSM data seem to be in between the results of both other higher-order turbulence models RSM and SST. For this reason, it was decided to use the fine mesh in combination with the EARSM model as the standard setup for the main numerical study.

The numerically studied test geometries correspond to extracted 2-D models of the experimentally studied configurations (see Fig. 4a), with a small difference in the length of the main plate, which was 400 mm. Another difference was how the position of the shock generator was varied. In contrast to the experiment, it was moved horizontally and not vertically with respect to the flat plate. The vertical distance between the surface of the main plate and the leading-edge tip of the shock generator was nominally kept constant at 80 mm throughout the present numerical investigations. An exception was the special numerical study that examined the influence of contour rounding instead of a sharp-edged kink at the impingement location (Fig. 4d). In this particular case, the vertical distance was 50 mm instead of 80 mm. Another special feature of this particular study was also the variation of bump length, because this was in the nature of the study. The total length of the bump was increased by the thickness of the intermediate layer L_1, which was used as a junction between the two analytically designed device halves. Details of this study and the geometries investigated will be discussed later.

The flow conditions investigated numerically are presented in Table 6. They are based on the conditions of wind-tunnel tests extended to additional simulations at a Mach number of 4.

III.   Results and Discussion

A.   Simplified Method for Concave-Bump Design

In this chapter, the analytical method [21] for preliminary design of a shock-canceling wall contour will be presented. According to the basic idea of this work touched on in the previous section, the concave bump initially causes a gentle increase of the pressure gradient at the beginning of the interaction zone. Near the maximum thickness, the pressure gradient is then nearly constant before it decreases gently to zero again further downstream. Two main effects contribute to this. On the one hand, the kink in the area of the shock impingement, which divides the concave bump into two halves, plays a very important role. The angle of surface inclination downstream of the impingement point should correspond as closely as possible to the nominal flow direction behind the impinging shock so that shock reflection does not occur. The second, but no less important, thing is the softly curved bump surface upstream and downstream of the expansion kink, inducing a continuous and isentropic flow compression along the wall as a basis for an advantageous pressure distribution. With these boundary conditions, there is nothing to say that a bump contour matched to the flow-deflection angle could not be universal for different Mach numbers. Of course, this is true as long as the flow-deflection angle remains truly constant.

First, let us take a closer look at the shape of a universal bump. The pressure increase due to an isentropic supersonic compression at infinitely small deflection $d\theta$ can be expressed using the well-known relation [6]

Table 3   Grid study for $M_1 = 3$ at $\beta = 12$ deg

Test case	Grid	Model	x_S, mm	x_R, mm	L_{sep}, mm	$L_{sep}/L_{sep,fine}$, %	$L_{sep}/L_{sep,ref}$, %
ref	coarse	EARSM	250.47	285.36	34.90	93.6	100.0
ref	medium	EARSM	249.05	285.41	36.36	97.5	100.0
ref	fine	EARSM	248.26	285.56	37.29	100.0	100.0
bump	coarse	EARSM	280.84	281.98	1.14	67.5	3.3
bump	medium	EARSM	280.23	281.94	1.71	100.7	4.7
bump	fine	EARSM	280.16	281.86	1.69	100.0	4.5

Table 4   Turbulence model study for $M_1 = 3$ at $\beta = 12$ deg

Test case	Grid	Turb. mod.	x_S, mm	x_R, mm	L_{sep}, mm	$L_{sep}/L_{sep,EARSM}$, %	$L_{sep}/L_{sep,ref}$, %
ref	fine	SA	266.74	290.76	23.99	64.3	100.0
ref	fine	RSM	250.08	283.51	33.43	89.7	100.0
ref	fine	EARSM	248.26	285.54	37.29	100.0	100.0
ref	fine	SST	251.95	290.46	38.50	103.2	100.0
bump	fine	SA	280.21	281.89	1.69	99.6	7.0
bump	fine	RSM	280.25	280.95	0.71	41.7	2.1
bump	fine	EARSM	280.16	281.86	1.69	100.0	4.5
bump	fine	SST	280.16	282.04	1.88	111.3	4.9

Table 5   Summarized bump effect at optimal impingement position

M_1	β, deg	$x_{imp,opt}$, mm	$\delta^{**}/\delta_{ref}^{**}$	$\bar{p}_{0,y}/\bar{p}_{0,y,ref}$	$L_{sep}/L_{sep,ref}$
2.5	6	283.8	0.975	1.029	0.000
3.0	6	282.9	0.974	1.027	0.000
4.0	6	284.4	0.967	1.046	0.000
5.0	6	284.6	0.993	1.023	0.000
2.5	8	284.5	0.895	1.084	0.000
3.0	8	283.1	0.909	1.077	0.000
4.0	8	283.7	0.934	1.103	0.000
5.0	8	284.0	0.974	1.079	0.000
2.5	10	285.4	0.753	1.185	0.000
3.0	10	284.7	0.811	1.210	0.000
4.0	10	285.6	0.885	1.236	0.017
5.0	10	285.8	0.955	1.143	0.004
2.5	12	285.6	0.691	1.263	0.000
3.0	12	284.9	0.759	1.327	0.000
4.0	12	285.5	0.863	1.328	0.015
5.0	12	285.9	0.937	1.213	0.000

$$\frac{dp}{p_{in}} = \frac{\gamma M_{in}^2}{\sqrt{M_{in}^2 - 1}} d\theta = K(\gamma, M_{in})d\theta \qquad (1)$$

Or, the increase of locally normalized pressure in this case is directly proportional to the growth of the deflection angle. So, the first insight is trivial, but very important. To obtain a desired distribution of the pressure gradient, it should simply be imposed on the deflection angle gradient. It is also remarkable that the proportionality factor K is only dependent on the local Mach number M_{in} if the heat-capacity ratio γ remains constant. In other words, the local pressure gradient on a given concave surface, which is normalized by locally determined wall-pressure level p_{in} and factor K, should be independent of the Mach number. Of course, this does not mean that the pressure distribution normalized by the freestream value p_1 is completely independent of the Mach number. Since the variations of the wall pressures and Mach numbers along a given curved streamline are still dependent on the initial Mach number, the normalized pressure distributions will in any case also show a Mach number dependence. A first idea of how great this influence in a standardized representation is can be derived directly from the results of the analytical study presented in the following section.

To obtain a generalized shock-canceling wall contour, an analytical 2-D study was conducted applying inviscid gas-dynamic relations to find the streamline pathway leading to a desired pressure distribu-tion. Based on Eq. (1), the normalized local deflection angle of the surface θ/θ_{max} was used to describe the bump contour as a function of the normalized longitudinal coordinate x/L. Here, θ_{max} is the maxi-mum deflection angle at the expansion kink, which corresponds to the given flow-deflection angle behind the impinging shock, and L is the half-length of the bump. For simplicity, a contour was sought that is symmetric with respect to the kink, since an asymmetric bump had not shown any particular advantages for nonviscous flows in a preliminary investigation. The bump contour before and after the kink was constructed analytically, alternatively using polynomial or power functions, to bring the resulting pressure distribution into agreement with the conditions discussed previously. Entire families of contour shapes were thus analyzed by varying the function param-eters and evaluated individually based on resulting distributions of pressure, pressure gradient, and its derivative. The bump contour finally found, which best meets the requirements, can be described analytically by means of the following pair of third-degree polyno-mial functions [21]:

$$\theta/\theta_{max} = 1.69(x/L)^2 - 0.69(x/L)^3, \qquad 0 \le x/L < 1 \qquad (2)$$

$$\theta/\theta_{max} = -1.69(2 - x/L)^2 + 0.69(2 - x/L)^3, \qquad 1 < x/L \le 2 \qquad (3)$$

Equation (2) describes here the normalized surface-deflection angle as a function of the normalized longitudinal coordinate for the first half of the bump, upstream of the kink. Considering that the contour is symmetric, Eq. (3) describes the bump contour downstream of the kink.

Figure 5a shows the variation of the normalized deflection angle along a concave-bump contour in accordance with the Eqs. (2) and (3). The resulting contour of the bump derived for the case with $\theta_{max} = 12$ deg and the expected shock and wave structure at an inflow Mach number of 3 are shown in Fig. 5b. The wave topology was calculated using the method of characteristics and corresponds to the case of an optimally positioned bump. This optimal position was determined iteratively by varying the shock impingement location with respect to the position of the bump. In the calculations per-formed, the isentropic compression was simulated by a limited number of very weak shock waves as resulting from a sequence of very small deflection angle steps ($\Delta\theta \le 0.06$ deg). This works well as long as the compressed flow remains supersonic. The waves presented here show only a small selection of the compression waves considered. Figure 5c shows additionally the distributions of the pressure coefficient c_p predicted for the set of investigated Mach numbers. It can be seen that the c_p distributions obtained for different Mach numbers are quantitatively different but qualitatively very
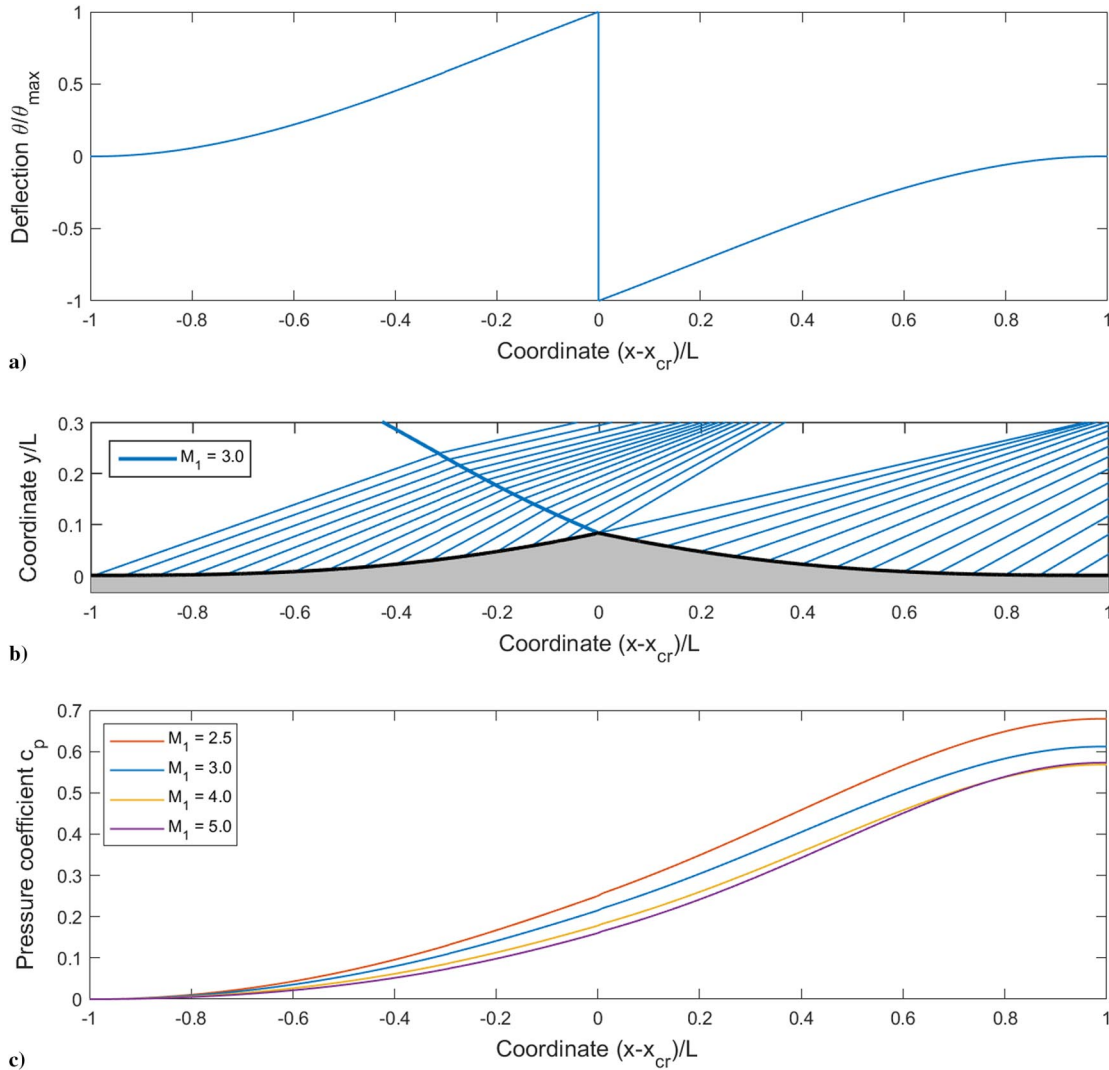
Fig. 5 a) Deflection-angle profile proposed, b) wave structure expected for $M_1 = 3.0$ at $\theta_{\max} = 12$ deg, and c) pressure distributions for different M_1 at $\theta_{\max} = 12$ deg.

similar. Accordingly, the insights gained so far allow us to remain optimistic. The announced detailed experimental and numerical verification of the design method, which follows in the next sections, is intended to show whether the conditions predicted actually apply and the proposed shock-control concept works also in viscous flow at Mach-number variation.

B. Validation of Numerical Results

As described earlier, the current study obtained numerous shadowgrams from the experiment but very limited wall-pressure data. To support the validity of the numerical simulations, we would like to refer to a comparable study [22] by the same research group, which includes a validation with more detailed experimental data. This study was performed at a Mach number of 3 and describes the interaction of an incident 2-D bow shock on the turbulent boundary layer. Similar to the present work, the numerical simulations were performed in the cited work with the DLR TAU code using the EARSM turbulence model. For the validation, not only boundary-layer parameters in the undisturbed turbulent boundary layer (velocity profiles, distributions of integral boundary-layer thicknesses, and skin-friction coefficient) but also detailed distributions of wall pressure and heat flux density in the interaction zone of the SWBLI were used.

An excerpt from [22] in Fig. 6 shows a comparison based on the detailed wall-pressure distributions of two different shock intensities. The selected cases H15-100 (green line) and J30-100 (blue line) correspond to shock intensities p_2/p_1 of 2.54 and 3.73,

respectively (see Table 2 of the original paper). The comparison shows that, overall, the predicted wall-pressure distributions reproduce the experimental distributions quite well. Also of interest to the present study is the interaction length L_{ui}, which is defined as the
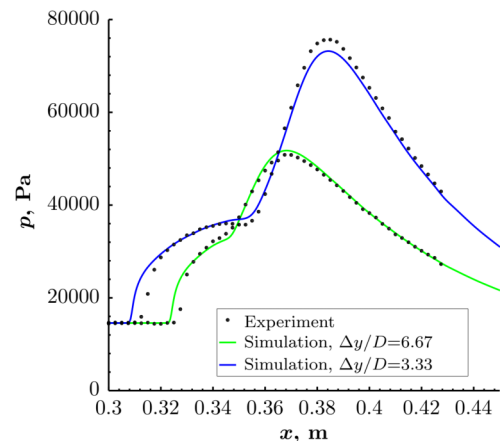

Fig. 6 Comparison of experimentally measured (black dots) and simulated (solid lines) wall-pressure distributions from [22] for the cases H15-100 (green line, $p_2/p_1 = 2.54$) and J30-100 (blue line, $p_2/p_1 = 3.73$) at $M_1 = 3$ (see Fig. 17b and Table 2 of the original work).

distance between the upstream-influence point and the shock-impingement point. An analysis of the data in Fig. 6 shows that L_{ui} is only slightly overestimated by the numerical simulations compared to the experiment. For L_{ui}, the discrepancies found in the original work were quantified with normalized deviations. The values were $\Delta L_{ui} = 4.47\%$ for the H15-100 case and $\Delta L_{ui} = 4.05\%$ for the J30-100 case. Compared to the uncertainties otherwise found in RANS simulations (see, e.g., Ref. [23]), the deviations found appear to be quite acceptable.

To explicitly evaluate the numerical results of the current study, the next step was to quantitatively compare the predicted interaction lengths L_{ui} of the reference flow (without bump) with some experimental datasets known from the literature. For this purpose, the scaling approach of [19] was chosen to allow a reliable comparison. This approach describes the scaled interaction length L^* as a function of the scaled interaction strength c_p^*, where both are defined as

$$L^* = \frac{L_{ui}}{\delta^*} \frac{\sin(\epsilon)\sin(\theta)}{\sin(\epsilon - \theta)} \quad (4)$$

$$c_p^* = c_p \left(\frac{Re_\delta}{2 \times 10^5}\right)^{-0.27(c_p)^{1.41}} \quad (5)$$

Here δ^* is the displacement thickness, ϵ and θ are correspondingly the impinging-shock and the flow-deflection angles, c_p ($= ((p_3/p_1) - 1)/(0.5\gamma M_1^2)$) is the pressure coefficient, and Re_δ is the Reynolds number based on the boundary-layer thickness. All parameters except L_{ui} correspond to the local undisturbed conditions at the virtual shock impingement position. It was demonstrated in the cited work that after scaling, the existing and obtained experimental data for oblique shock waves impinging on a turbulent boundary layer form a common and reliable dependence in a very wide range of shock intensities.

A joint representation of the numerical data from the current work, including only the RANS simulations of the reference flow (without the bump), is shown in Fig. 7 according to the scaling approach described in the previous section. The symbols differ by shock-generator angle β, and the symbol colors are sorted by Mach number M_1. For the scaling of the interaction length with Eqs. (4) and (5), the true local flow-deflection angle θ_{imp} and the reflected shock intensity p_3/p_1 were used. The latter was determined using a simulation with a shock generator but without the flat plate at the vertical position where the flat plate would actually be. These values are documented in the legend of Fig. 7 for each combination of incoming-flow Mach number M_1 and shock-generator angle β studied. The angle θ_{imp} is in most cases, as expected, slightly higher than the shock-generator angle β due to the displacement effect of the shock-generator boundary layer. The exception at $M_1 = 5$ is an effect of the expansion waves, originating from the trailing edge of the shock generator.

The reduced scatter of the data within the individual point clouds consisting of identical symbols and colors (constant Mach number and shock-generator angle) obviously describes their good reproducibility regardless of the Reynolds number or x_{imp} variation present. Although the current numerical data show a tendency to slightly overestimate the interaction length, they follow the empirical path from [19] (black star symbols) quite well. The reliability of the numerical results can thus be considered as sufficient, considering the objectives of the present study.

C. Potential of Concave Bumps for Separation Control

The main results presented and discussed in this section were obtained numerically in wide variation ranges of Mach number ($M_1 = 2.5$, 3.0, 4.0, and 5.0) and shock-generator angle ($\beta = 6$, 8, 10, and 12 deg). Such extensive variations in flow conditions were chosen to cover the entire relevant range of real supersonic diffusors and to extensively test the applicability of the flow control device for those conditions. For each combination of Mach number and shock-generator angle considered in this numerical study, the shock impingement position x_{imp} was systematically varied (between about 250 and 310 mm), while the bump geometry and the absolute x coordinate of the bump crest/kink $x_{cr} = 280$ mm were kept constant. Experimental results were obtained only at selected combinations of Mach numbers and shock-generator angles and were mainly used for qualitative verification of the numerically identified trends. For this purpose, not only the experimental shadowgrams were used but also

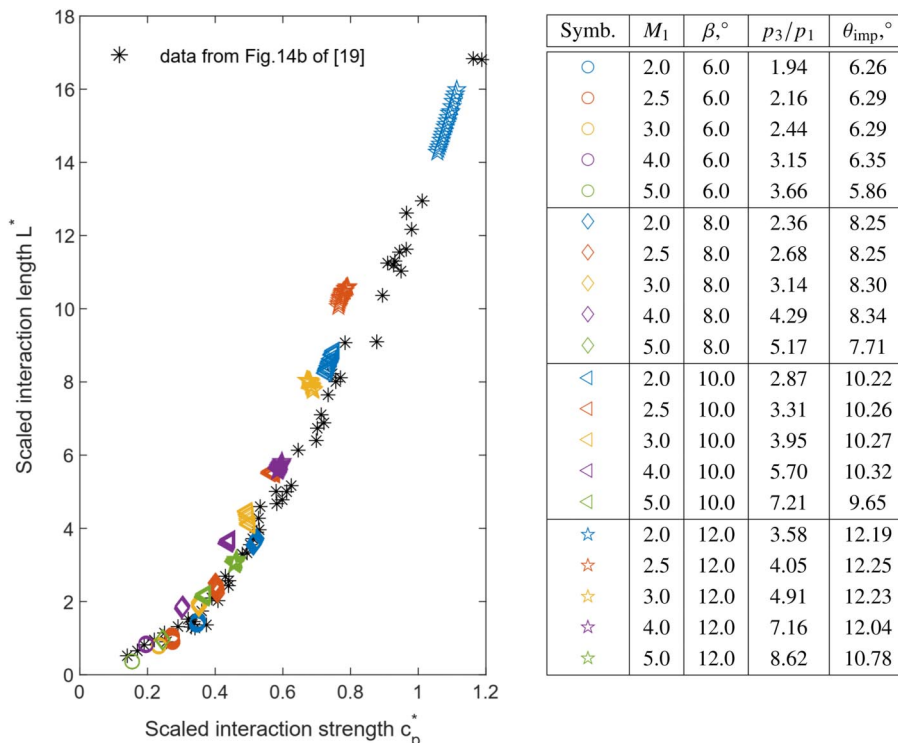| Symb.	M_1	$\beta,°$	p_3/p_1	$\theta_{imp},°$
○	2.0	6.0	1.94	6.26
○	2.5	6.0	2.16	6.29
○	3.0	6.0	2.44	6.29
○	4.0	6.0	3.15	6.35
○	5.0	6.0	3.66	5.86
◇	2.0	8.0	2.36	8.25
◇	2.5	8.0	2.68	8.25
◇	3.0	8.0	3.14	8.30
◇	4.0	8.0	4.29	8.34
◇	5.0	8.0	5.17	7.71
◁	2.0	10.0	2.87	10.22
◁	2.5	10.0	3.31	10.26
◁	3.0	10.0	3.95	10.27
◁	4.0	10.0	5.70	10.32
◁	5.0	10.0	7.21	9.65
☆	2.0	12.0	3.58	12.19
☆	2.5	12.0	4.05	12.25
☆	3.0	12.0	4.91	12.23
☆	4.0	12.0	7.16	12.04
☆	5.0	12.0	8.62	10.78

Fig. 7 Comparison of results obtained numerically in the current work (color symbols, see legend) with a variety of experimental results available for 2-D impinging SWTBLI (black star symbols, as shown in Fig. 14b of [19]) according to scaling approach for the interaction length presented in [19].

a) $M_1 = 2.5$

b) $M_1 = 3.0$
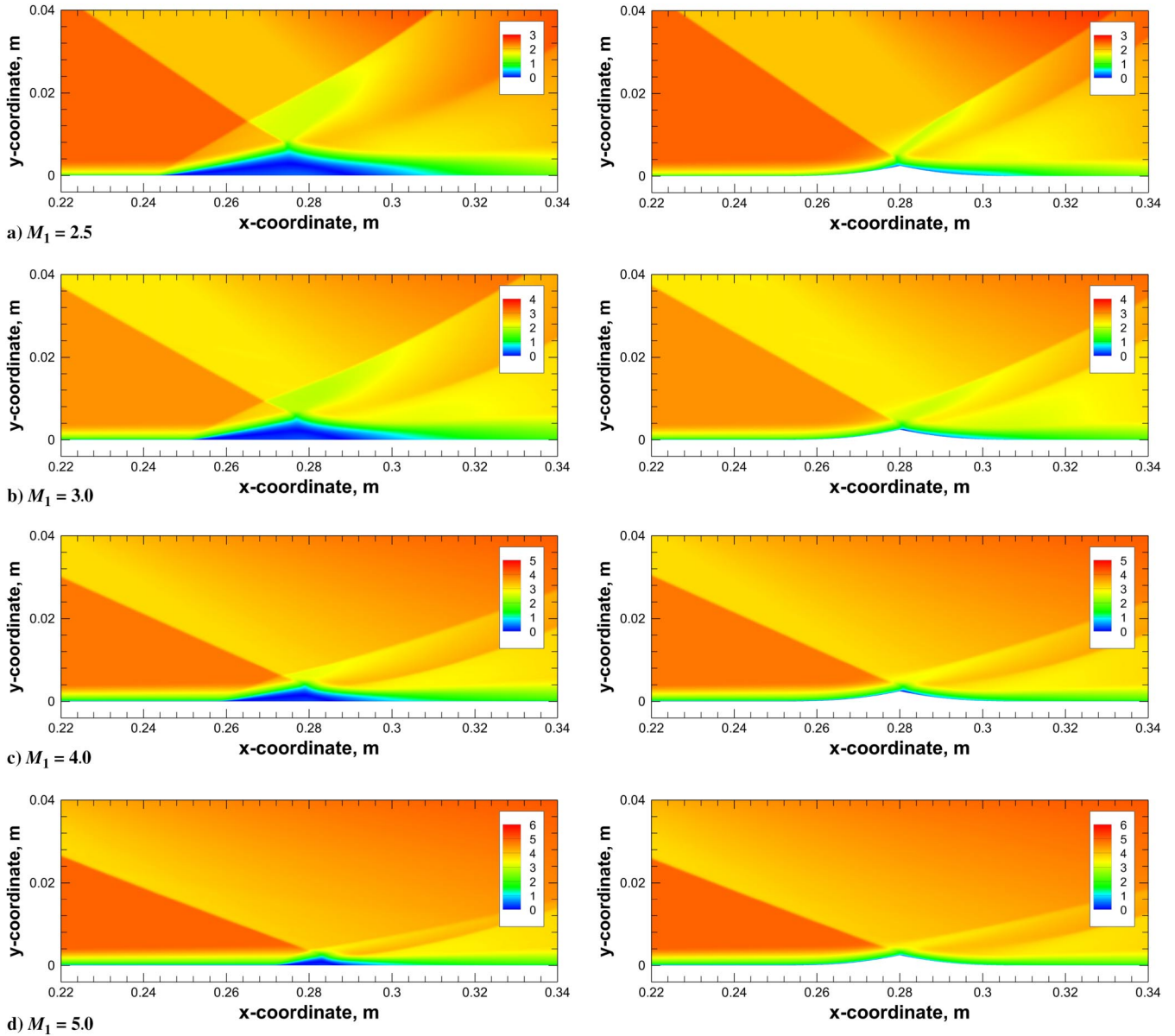
c) $M_1 = 4.0$

d) $M_1 = 5.0$

Fig. 8   Numerical Mach-number distributions for (left) the reference cases and (right) cases controlled by a concave bump with $\theta_{\max} = 12$ deg at $\beta = 12$ deg.

the mean-wall-pressure levels measured at two pressure taps immediately upstream and downstream of the crest of the bump.

Figures 8 and 9 show Mach number distributions and numerical shadowgrams predicted for different M_1 at $\beta = 12$ deg both characterizing the flow topology with and without the concave bump. To clearly distinguish the predicted recirculation bubbles from the rest of the flowfield in Fig. 9, the recirculation regions $u<0$ were colored blue. This helps to get a clear picture. As expected, the initial size of the separation bubble in the reference cases (images on the left) decreases with increasing Mach number (see, e.g., [18,19]). Examining now the test cases with concave bump (images at the right), it can be seen that an optimally positioned bump suppresses the separation bubble very effectively. This goes along with a significant change in the wave structure. For example, the compression waves induced on the windward side of the bump combine to form a shock wave only at a much greater distance from the wall than is the case with the separation shock in the reference flow.

A similar effect of the concave bump can be observed in the experimental shadowgrams (Fig. 10), which visually confirm the mentioned suppression of the length of the interaction zone and the transformation of the reflected/induced shock waves. The results shown

were obtained for each individual case for an optimal position of the bump with respect to the incident shock front.

However, caution must be taken when interpreting experimental shadowgrams. If, as expected, the numerical shadowgrams directly show the derivative of the density gradient in the flowfield, the conventional experimental shadowgrams strictly visualize the resulting displacement of light rays due to refractive index gradients along the entire ray path [24]. First of all, this means that in the experimental shadowgrams, even objects that are far away from each other and are in the beam path can be imaged equally clearly. Thus, the shadows of shock waves from the outer edges of the test area are usually just as present on them as those from the core flow under investigation. In Fig. 10b, for example, a shock was identified and marked with the help of a red line, which most likely originates at the lateral edge of the flat plate and thus lies outside the 2-D flow region. Another peculiarity of the experimental shadowgrams is secondary optical disturbances of various kinds, which can be easily misinterpreted. In the images from Fig. 10, for example, typical spot artifacts (so-called caustics) can be seen, which result from the crossing of light rays near strongly curved shear-layer edges or shock fronts.
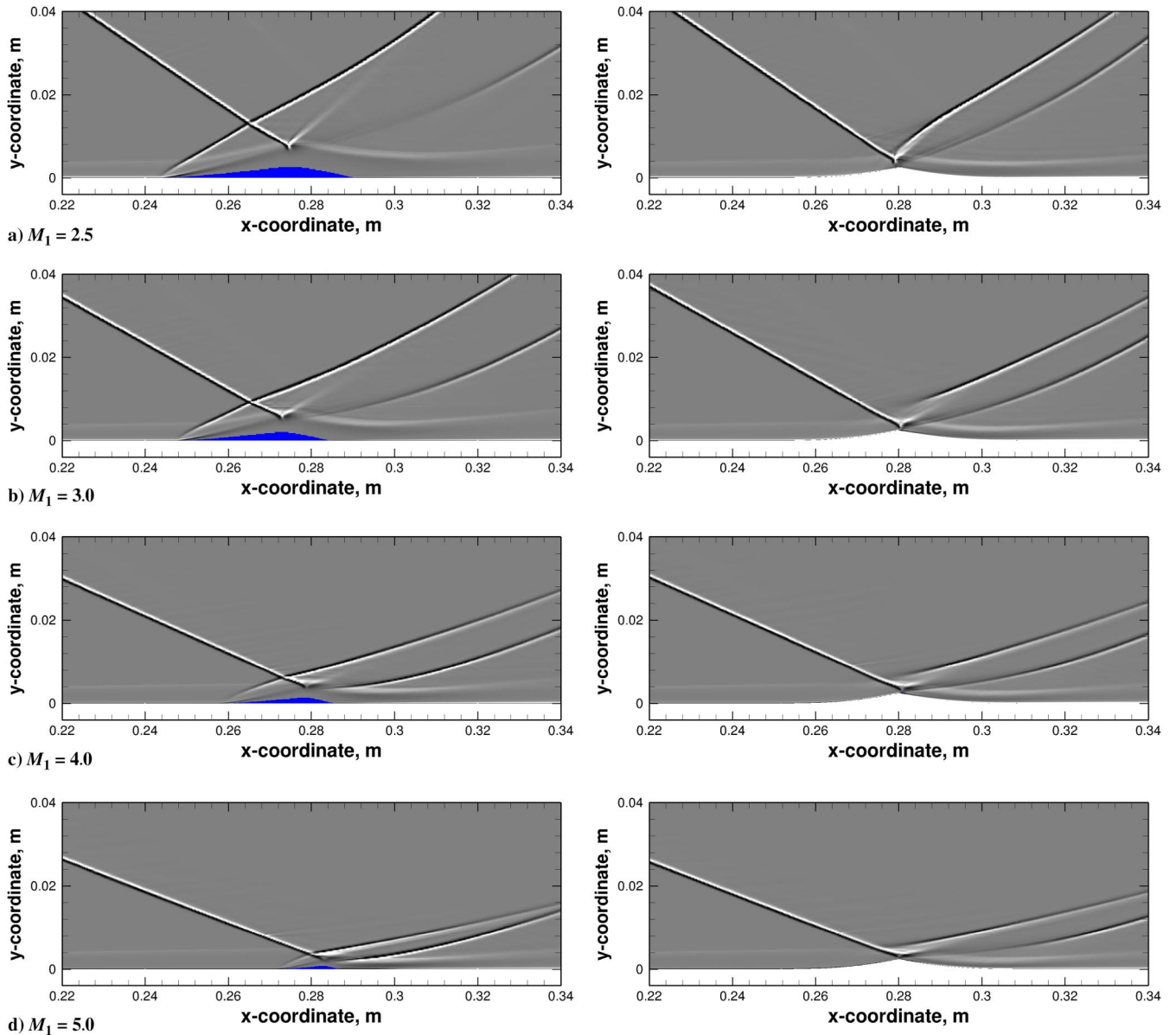
a) $M_1 = 2.5$

b) $M_1 = 3.0$

c) $M_1 = 4.0$

d) $M_1 = 5.0$

Fig. 9   Numerical shadowgrams (grayscale) for (left) the reference cases and (right) cases controlled by a concave bump with $\theta_{max} = 12$ deg at $\beta = 12$ deg. The areas colored in blue correspond to a reverse flow component $u < 0$ predicted in the flowfield.

An important effect of a bump, visible to the naked eye in the numerical and experimental shadowgrams, is the reduced boundary-layer thickness at the right edge of the images compared to the reference case. This phenomenon is clearly confirmed quantitatively when comparing numerical data in Fig. 11. Here, the numerically calculated total-pressure profiles, velocity profiles, and Mach-number profiles are shown in situations with and without bump for a single test case at the most downstream flat plate location of $x = 400$ mm. It is obvious that not only the thickness of the decelerated near-wall layer but also the profiles of individual parameters indicate integral reduction of losses. All these features confirm a positive effect of the well-positioned concave bump, which in its turn is obviously due to the carefully executed isentropic flow compression along the wall.

Selected wall-pressure and skin-friction distributions for the test case with $M_1 = 3$ and $\beta = 10$ deg, which are compared in Fig. 12a for the reference case a and in Fig. 12b for the case with a corresponding concave bump, can help to better understand the operating principle of a concave bump with variation of the shock impingement position. Of particular importance here is the optimum shock-impingement position $x_{imp,opt}$ (black line), which comes closest to a desired direct impact of the shock front on the crest of the bump.

This optimal position was automatically determined here based on the calculated skin-friction distributions from the entire set of shock impingement locations examined. The strategy used exploited the well-known fact that the suppression of the separation bubble is reflected in a weakening of the reverse flow intensity. Specifically, the local minimum in the skin-friction distribution along the interaction region $c_{f,min}$ was compared for different shock impingement locations to automatically identify the $x_{imp,opt}$ where $c_{f,min}$ was highest.

From these data, it is easy to see that SWBLI leads to an extended separation bubble in the reference case (Fig. 12a), which increases slightly with an increasing x_{imp} coordinate. As already shown by the scaling of the interaction length in Fig. 7, the variation of the interaction length (and thus also the length of the separation bubble) corresponds to the variations of the local displacement thickness and the local Reynolds number. The use of a bump (Fig. 12b) adds significantly more diversity. The optimal shock impingement position (black line) stands out in particular. Since the skin-friction coefficient remains positive throughout in this case, no recirculation bubble apparently arises in this case in the numerical simulation. The corresponding wall-pressure distribution can be compared quite well, except for a short region in the immediate vicinity of the crest, with
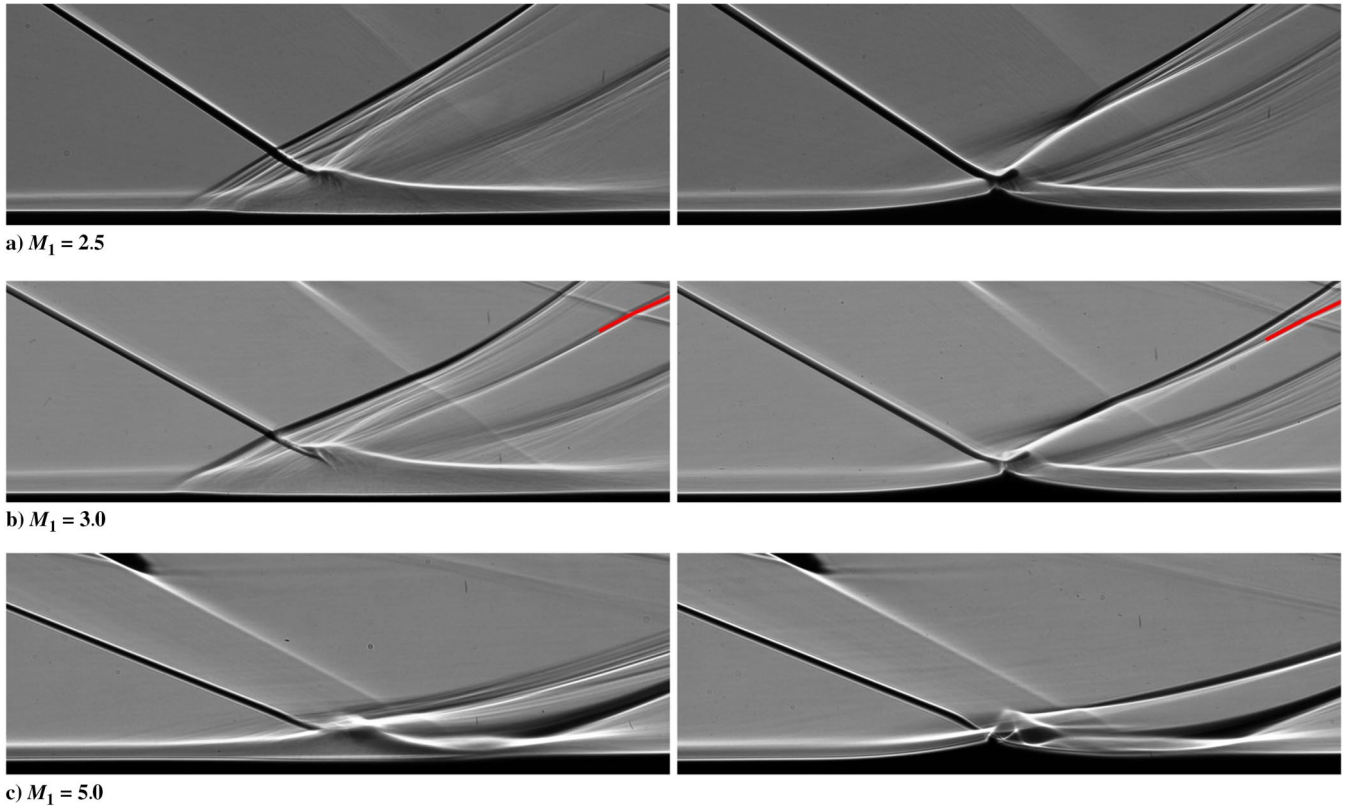
a) $M_1 = 2.5$

b) $M_1 = 3.0$

c) $M_1 = 5.0$

Fig. 10 **Experimental shadowgrams for (left) the reference cases and (right) cases controlled by a concave bump with $\theta_{\max} = 12$ deg at $\beta = 12$ deg.**
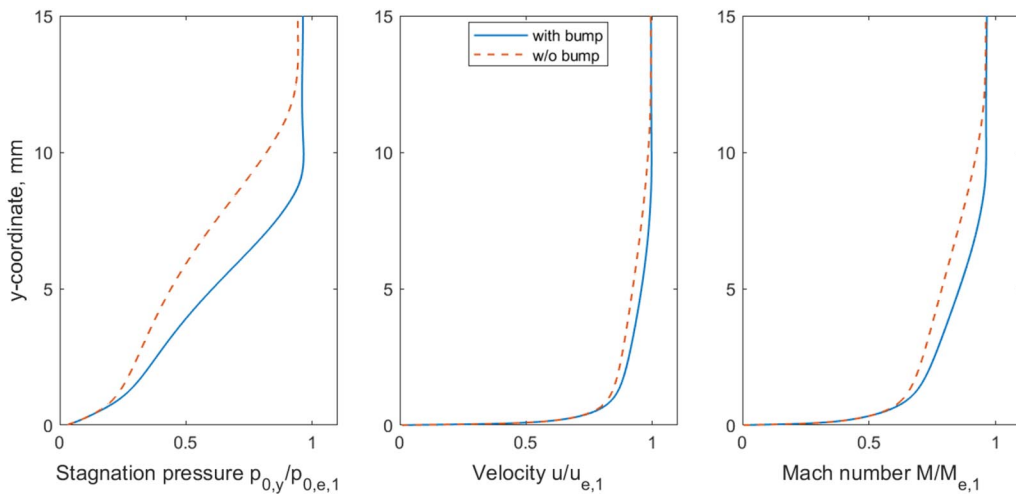

Fig. 11 **Effect of the concave bump at optimum shock-impingement location on (left) the normalized stagnation pressure profile $p_{0,y}/p_{0,e,1}$, (middle) velocity profile $u/u_{e,1}$, and (right) Mach number profile $M/M_{e,1}$ for a test case with $M_1 = 3$ at $\beta = 12$ deg.**

the straightened course of a rounded ramp. The bump appears to work well in this case. However, when deviating from the $x_{\mathrm{imp,opt}}$ coordinate, the positive bump effect decreases rapidly. The quantitative effect of this "off-design" shock impingement will be discussed in the following section.

To verify the application of the simplified method for the design of the bump, Fig. 13 shows the calculated wall-pressure distributions along the bump with $\theta_{\max} = 12$ deg for different Mach numbers at a shock-generator angle of 12 deg. In each case, the red line presents the surface pressure distribution of the optimal positioned bump, and the dashed black line shows the initial distribution for the reference case without bump, both predicted numerically by RANS computations. The purple lines correspond to special RANS–Euler calculations, which were additionally performed to show the influence of the expansion waves on the incident shock front. The RANS simulations

were repeated here, changing only the boundary condition at the flat plate with the bump from a no-slip to a Euler-wall condition. Thus, these simulations still show a realistic incident shock front (with $\theta \neq \mathrm{const}$) that initially arises with a "full viscous" flow around the shock generator, thereupon impinges almost optimally on a frictionless contoured wall, and is subsequently reflected without SWBLI. The blue line shows the pressure distribution predicted by the method of characteristics that occurs in a nonviscous flow when an idealized plane shock wave with a fixed flow-deflection angle of $\theta = 12$ deg impinges on the optimally positioned bump. As before, θ_{imp} corresponds to the actual local flow-deflection angle at the virtual shock impingement location (see legend in Fig. 7).

It can be seen that the RANS-predicted pressure distributions deviate more and more from the simplified idealized prediction as the Mach number increases. There are two different mechanisms that lead to this.
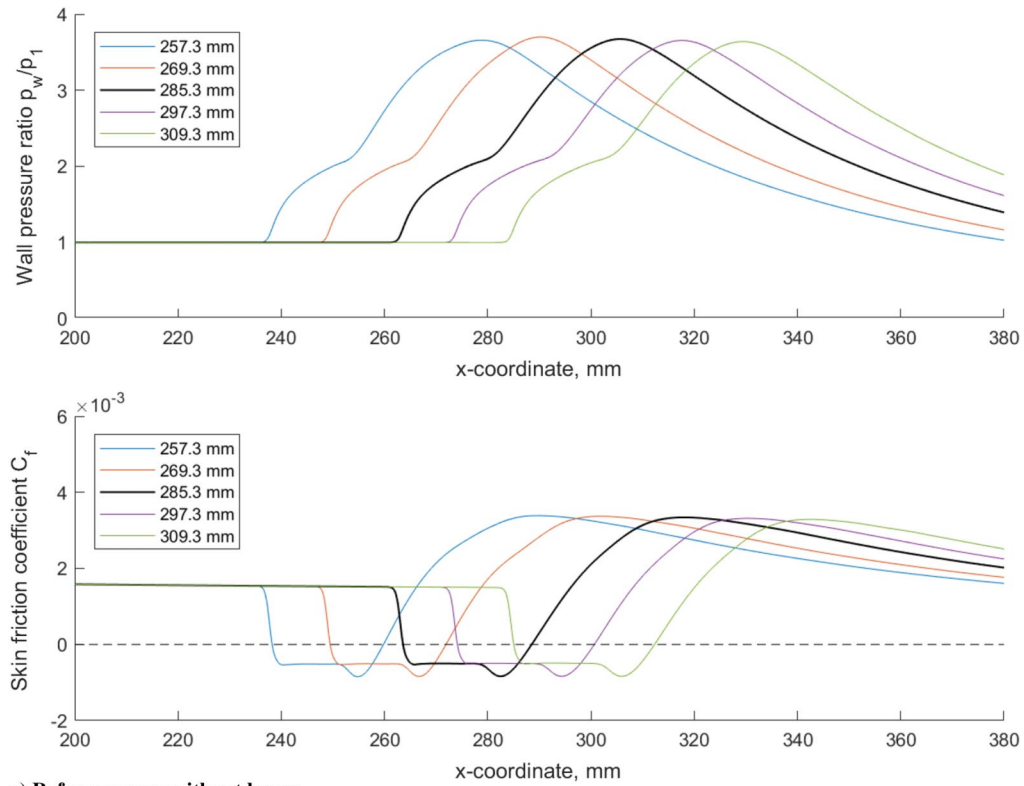
a) Reference case without bump
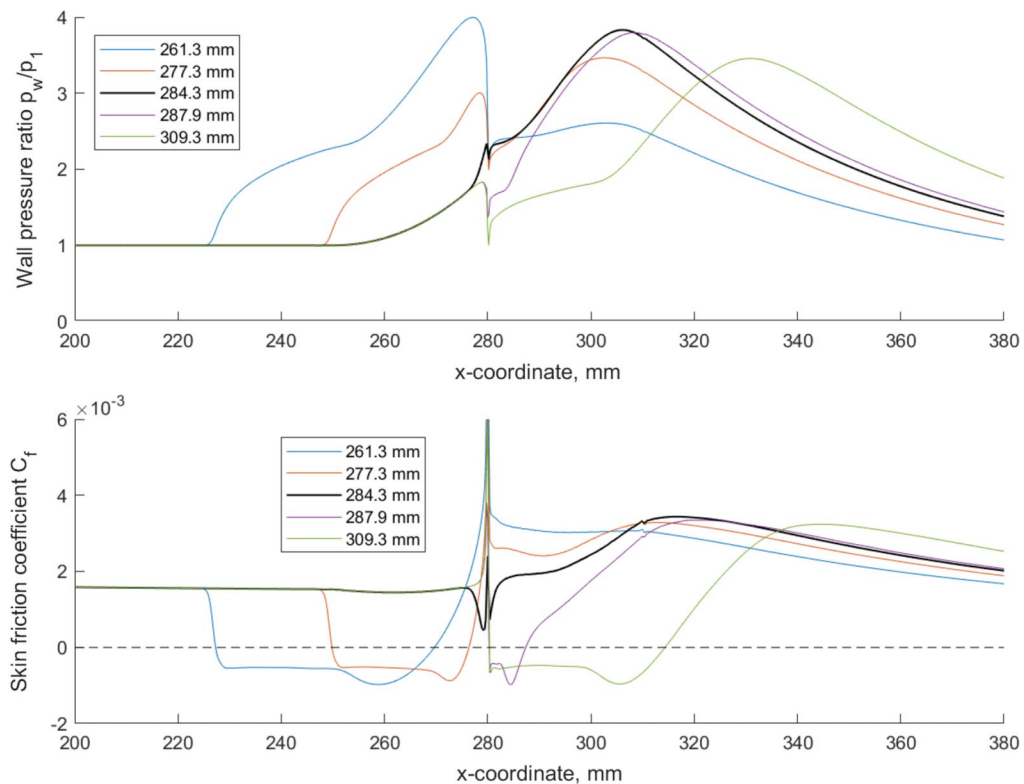
b) Case controlled by a concave bump ($\theta_{max} = 10°$, $x_{cr} = 280$ mm)

Fig. 12   Wall-pressure and skin-friction distributions for selected shock-impingement positions x_{imp} (legend) at $M_1 = 3$ and $\beta = 10$ deg.

The first is the effect of the finite length of the shock generator on the wall-pressure distribution. The expansion waves generated at the trailing edge of the shock generator lead to a considerable weakening of the impinging shock front on its way to the plate, as well as inevitably to the influence of the entire interaction area. This effect increases with the increase of the Mach number. At the highest Mach number of 5, this effect is most pronounced. The negative pressure jump at the expansion kink predicted in the RANS–Euler calculation for this case is a consequence of the weakened shock wave. Strictly speaking, at the highest Mach number, the designed bump contour $\theta_{max} = 12$ deg no longer matches the incident shock wave $\theta_{imp} = 10.78$ deg, and the device is not able to develop maximum effectiveness.
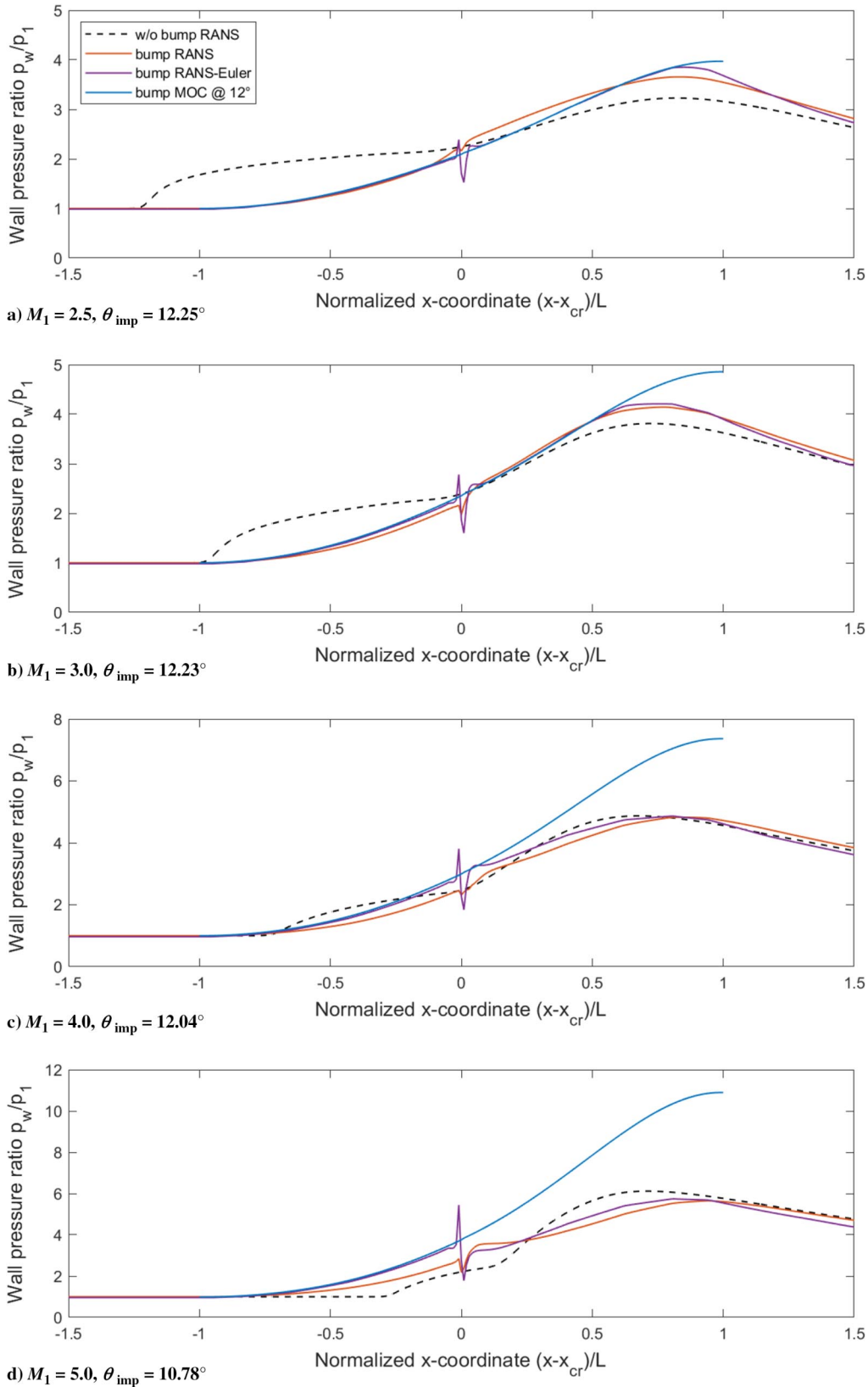
a) $M_1 = 2.5$, $\theta_{imp} = 12.25°$

b) $M_1 = 3.0$, $\theta_{imp} = 12.23°$

c) $M_1 = 4.0$, $\theta_{imp} = 12.04°$

d) $M_1 = 5.0$, $\theta_{imp} = 10.78°$

Fig. 13   Concave-bump effect on the pressure distribution for different Mach numbers with $\beta = 12$ deg at $\theta_{max} = 12$ deg.

The second reason why the simplified predictions overestimate the pressure distributions determined by the full RANS simulations is the neglect of the boundary layer on the contour bump. Due to viscosity-induced displacement of the external flow in RANS simulations, a systematic increase in pressure along the bump causes a complex deformation of the effective displacement body, which deviates from the fixed bump contour. This effect means a delayed increase of the

wall pressure in the realistic viscous flow (red line) compared to the simplified gas dynamic consideration (blue line) and Euler-wall simulations (purple line). The data presented show that the distance between the aforementioned wall-pressure distributions on the windward side of the bump increases with increasing inflow Mach number, so that the need for adequate correction of the simplified design procedure becomes most apparent there.

To allow quantitative comparison of the bump effectiveness at various shock impingement locations, the positions of the separation and reattachment points x_S and x_R, as well as the resulting length of the separation bubble $L_{\mathrm{sep}} = x_R - x_S$, were determined from the numerical data. Figure 14 shows the evolution of these parameters with variation of the shock impingement location for a selected test case, which is representative for the other combinations of M_1 and θ investigated. The coordinates x_S and x_R correspond here, as usual, to the local condition with $c_f = 0$ provided an uninterrupted reverse flow between these points could be detected. It can be clearly seen that when the optimal impingement location is reached (here $x_{\mathrm{imp,opt}} \approx 284.4$ mm), the existing separation bubble is suppressed for the most part. It is plausible that in this process the separation and reattachment points approach the bump crest accordingly, so that the condition $x_S = x_R = x_{\mathrm{cr}}$ holds asymptotically there. As expected, the optimal shock locations do not automatically correspond to the situation $x_{\mathrm{imp}} = x_{\mathrm{cr}}$ but deviate somewhat from it. This deviation is due to the protruding bump contour and because of the shock-front curvature as it penetrates the boundary layer (see, e.g., [13]). These effects were not considered in the definition of the shock impingement location x_{imp}. The distance $\Delta x = x_{\mathrm{imp}} - x_{\mathrm{cr}}$ is only a few millimeters and thus has the order of magnitude of the local boundary layer thickness.

As mentioned, the sensitivity of the pressure values at two discrete measurement points p_A and p_B close to the crest of the wind-tunnel model was used to verify the findings obtained from the numerical simulations. Figure 15 shows the evolution of these pressure values as well as its difference $\Delta p_{\mathrm{BA}} = p_B - p_A$ with the variation of the shock impingement location for the same test configuration as in Fig. 14. The numerical results (blue symbols) are presented there next to the experimentally determined data (red symbols). The range of fluctuations during the test series, which in each case was greater than the reported measurement accuracy of the pressure measurement sensors, is shown in the plot by means of error bars for each individual measurement point. It can be seen that, qualitatively, the experimentally recorded tendencies agree very well with the numerical ones. Of particular note is the specific progression of Δp_{BA} near the optimal shock impingement location,

which is reproduced very similarly in both datasets. The achievement of a positive maximum in this region was expected from the desired nonviscous pressure distribution along the bump when the shock front directly hit the bump crest. However, there are also systematic deviations in the courses of experimental and numerical data over x_{imp}, for which we have no clear explanation so far. The somewhat different configurations of the wind-tunnel model and the numerical model are the most plausible explanation we have at the moment. A thorough review of this discrepancy is planned in the medium term using detailed pressure measurements on the wind-tunnel model.

For a uniform consideration of the effect of a Mach number variation with a fixed contour bump, further evaluation criteria are derived for the cases with nominally $\beta = 12$ deg (at $\theta_{\mathrm{max}} = 12$ deg) in a normalized form in Fig. 16. Figure 16a, the separation-length ratio $L_{\mathrm{sep}}/L_{\mathrm{sep,ref}}$, Fig. 16b, the boundary-layer momentum-thickness ratio $\delta^{**}/\delta^{**}_{\mathrm{ref}}$, and Fig. 16c, the total-pressure-recovery ratio $\bar{p}_{0,y}/\bar{p}_{0,y,\mathrm{ref}}$, were each determined from the RANS data as a relationship to the respective reference value (without bump). The parameter ratios $\delta^{**}/\delta^{**}_{\mathrm{ref}}$ and $\bar{p}_{0,y}/\bar{p}_{0,y,\mathrm{ref}}$ (see Nomenclature for more details) were determined in each case at a fixed x coordinate of 400 mm within a near-wall layer of 8 mm.

According to the presented data, the concave bump has an overall positive effect on the induced separation bubble in an extended region around the optimal shock impingement location. In the specific example for the case $M_1 = 2.5$ and $\beta = 12$ deg (Fig. 16), the optimum shock impingement position is at about $x_{\mathrm{imp}} \approx 286$ mm, and the range with positive flow influence extends from about 273 to about 321 mm. Outside this range, the existence of a concave bump is rather counterproductive because it significantly enhances the initial separation bubble and thus leads to higher losses in the flow. If we take the normalized length of the separation bubble as a measure of the effectiveness of the device, the change in the positions of the separation and reattachment points can contribute quite a bit to understanding its functionality (see, e.g., Fig. 14b). The extent to which a deviation from the optimal impingement location affects the effectiveness of the bump depends not only on the size of the deviation but also on the direction. In this context, a deviation of
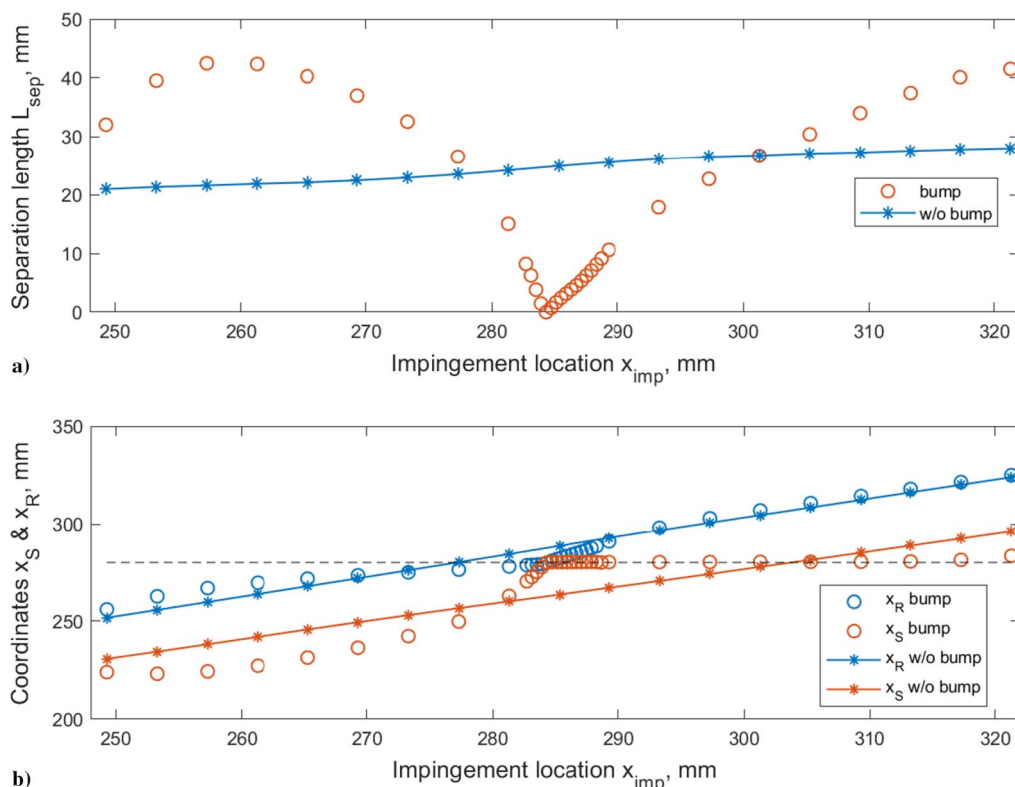

Fig. 14 Evolution of the separation-bubble length and coordinates of the separation and the reattachment with variation of shock-impingement locations x_{imp} for the case $M_1 = 3.0$ and $\beta = 10$ deg.
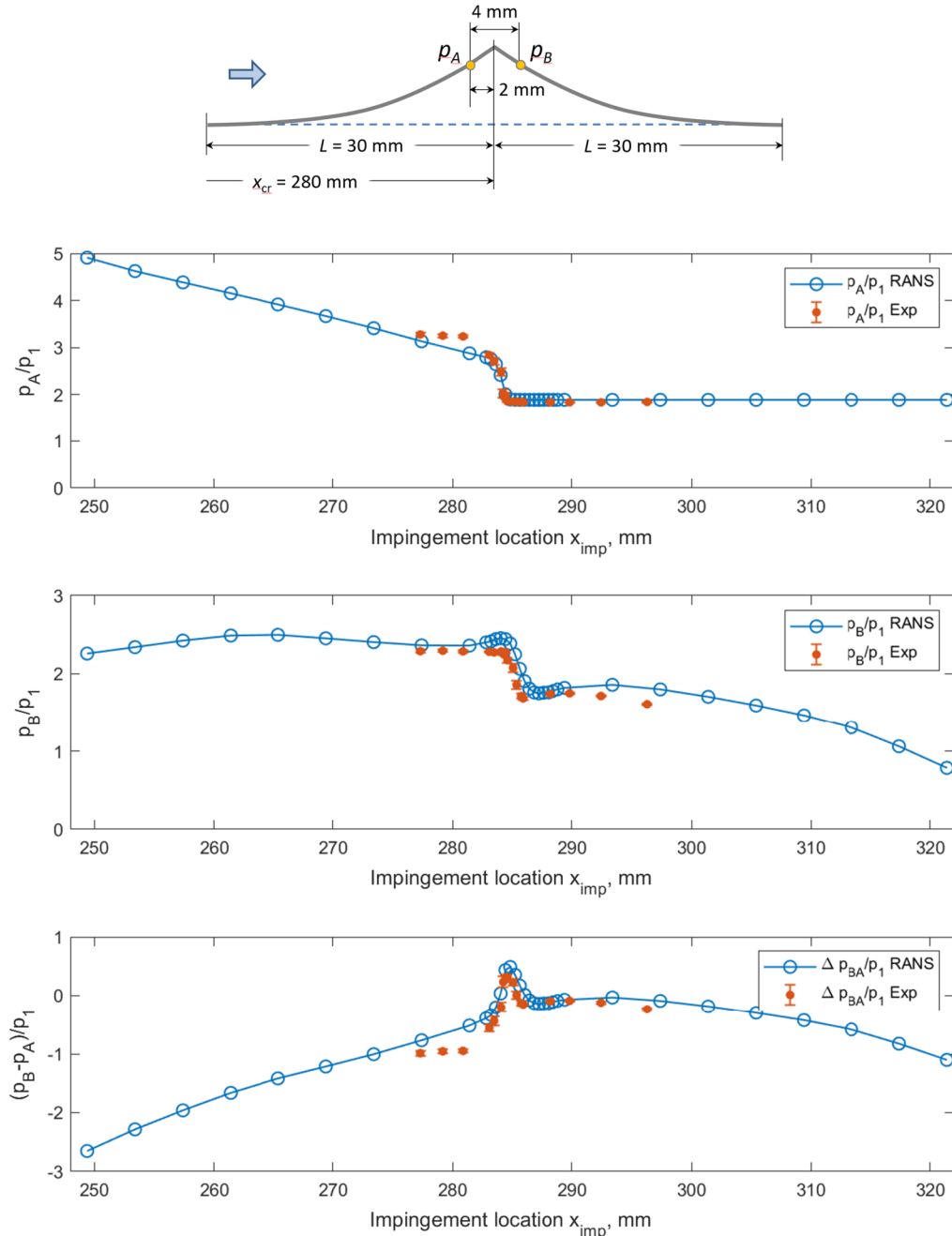
Fig. 15   Local wall-pressure evolution with variation of shock-impingement locations x_{imp} for the case $M_1 = 3.0$ and $\beta = 10$ deg.

the same size in downstream direction is more favorable that in upstream direction. Or, in other words, the region of positive interference downstream of the optimal impingement point is much more extended than in the opposite direction. This seems to be plausible from a gas-dynamic point of view, but the interaction of the separation and reattachment points with the bump crest explains this very clearly. If the shock impingement location moves to the leeward side of the bump, the separation seems to be damped and the separation point is fixed at the crest/kink. The reattachment point behaves completely inconspicuously. This effect is desirable as long as the separation-length ratio remains below 1. However, when the shock impingement location moves to the windward side of the bump, the intensity of the interaction increases immediately, so that the separation bubble grows very quickly, and, compared to the reference case, the separation point is located much further upstream.

In summary, regardless of Mach number, the optimally positioned bump resulted in a reduction in separation length L_{sep} of up to 100% in the numerical simulations. For the other two parameters, which were

determined in each case at a fixed x coordinate of 400 mm within a near-wall layer of 8 mm, the gains are Mach number-dependent. Thus, the maximum reduction in momentum thickness of up to $\approx 31\%$ is achieved at $M_1 = 2.5$, and a maximum increase in total pressure recovery of up to $\approx 33\%$ is achieved at moderate Mach numbers of 3 and 4. At $M_1 = 5$, on the other hand, the smallest gains are captured, which is probably due to the discussed reduction of the flow-deflection angle along the shock front at this Mach number. The quantitative results on the effect of an optimally positioned bump are summarized in Table 5.

In an additional study, instead of the ideal sharp-edged kink, the effect of a rounded bump crest was investigated numerically at constant flow conditions for the case $M_1 = 3$ and $\beta = 12$ deg. Figure 17a shows a sketch of the studied model configuration. In this study, the total length of the bump was increased by the thickness of the intermediate layer L_1, which serves as a steady transition between the two previously defined halves of the bump. The contours of the two concave halves of the bump still correspond to Eqs. (2) and (3). The smooth transition between the two halves of
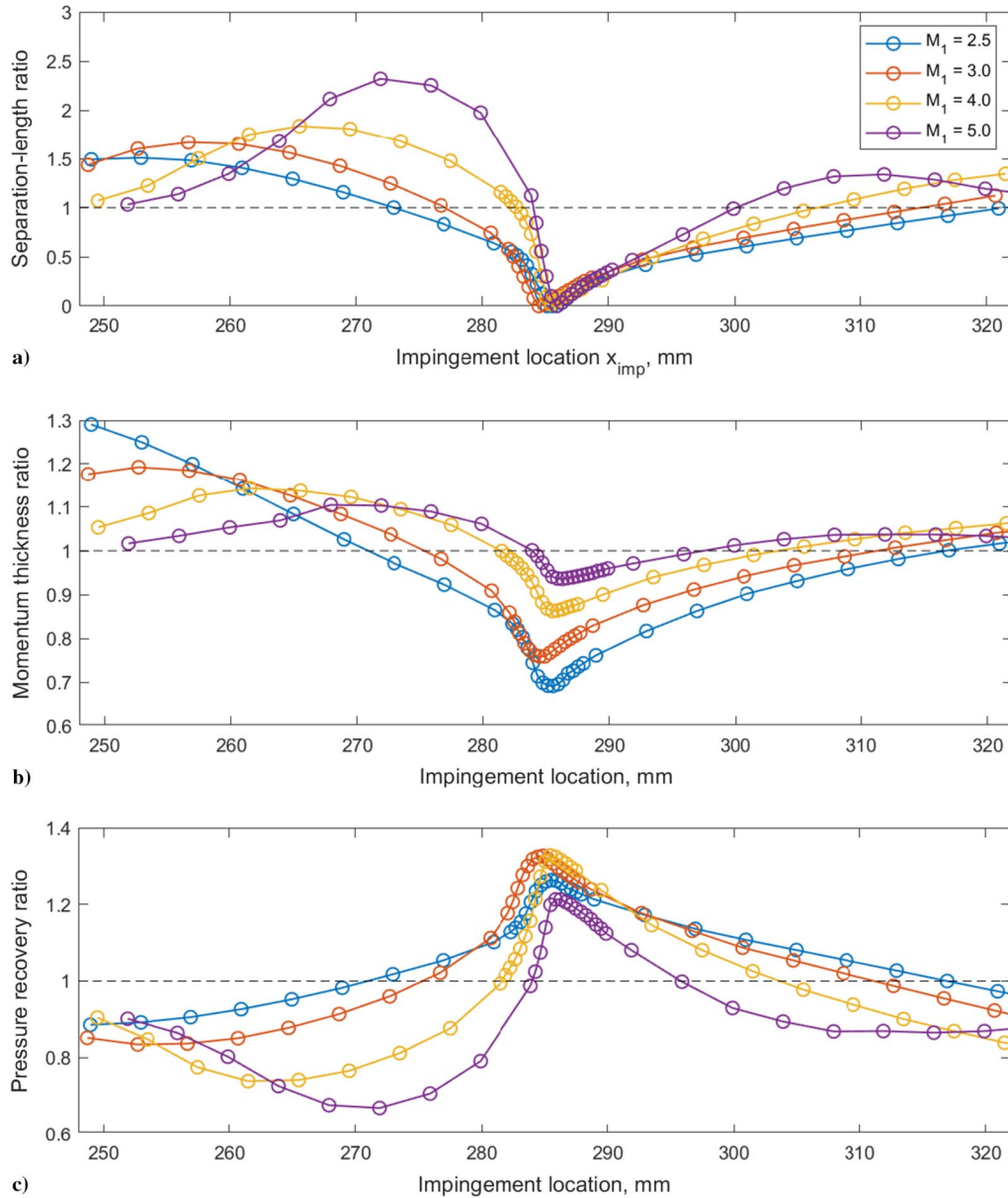
Fig. 16   Concave-bump effect on the a) separation-length ratio $L_{sep}/L_{sep,ref}$, b) momentum-thickness ratio $\delta^{**}/\delta^{**}_{ref}$, and c) total-pressure-recovery ratio $\bar{p}_{0,y}/\bar{p}_{0,y,ref}$ for different x_{imp} and Mach numbers at $\beta = 12$ deg.

Table 6   Flow conditions investigated numerically

M_1	$Re_{unit,1}$, 10^6 m^{-1}	p_0, MPa	T_0, K	p_1, Pa	T_1, K	U_1, m/s	ρ_1, kg/m^3
2.5	26.0	0.2324	268.0	13,602	119.1	547.2	0.39747
3.0	26.0	0.3000	268.0	8167	95.7	588.6	0.29700
4.0	26.0	0.4880	268.0	3214	63.8	640.8	0.17530
5.0	26.0	1.5200	411.0	2907	68.7	829.7	0.14720

the bump is in the form of an arc, which performs a change of the angle of inclination from θ_{max} down to $-\theta_{max}$. The radius of the arc R_1 is thus uniquely defined by L_1 and θ_{max} and can be easily determined from $R_1 = L_1/(2\sin(\theta_{max}))$. The variation of L_1 in this study from zero to 9 mm (30% of L) implies a variation of R_1 from zero to about 43 mm at $\theta_{max} = 6$ deg or to about 21.6 mm at $\theta_{max} = 12$ deg. Putting these radii in relation to the mean undisturbed boundary-layer thickness at the bump-crest coordinate $x_{cr} = 280$ mm for all Mach numbers investigated $\delta_{cr} \approx 3.6$ mm, the

maximum normalized radii R_1/δ_{cr} reached are about 12 and 6, respectively.

Figure 17b shows the final results of this study as the separation-length ratio versus the shock impingement location for the case $M_1 = 3$ and $\beta = 12$ deg. It is pleasing that the function of the bump is still retained even if the rounding radius is increased. However, its effectiveness slightly decreases. Indeed, in the case shown here, a generous increase in the normalized radius R_1/δ_{cr} results in only a moderate decrease in the effective separation-length reduction. Thus, rounding off the kink edge is definitely an option because it could improve the robustness of the solution and facilitate its technical implementation.

A final remark in conclusion: although the present study showed complete suppression of separation in most cases at the optimal point of impact, the lower end of the Mach number range studied also recognized the limits of effectiveness. For example, an attempt to extend the Mach number range of the numerical study to $M_1 = 2$ had shown that, for the strongest interaction case with $\beta = 12$ deg, the separation bubble could only be suppressed somewhat (results not presented here). The reason here was obviously the initial size of the separation bubble (without bump), which was significantly greater
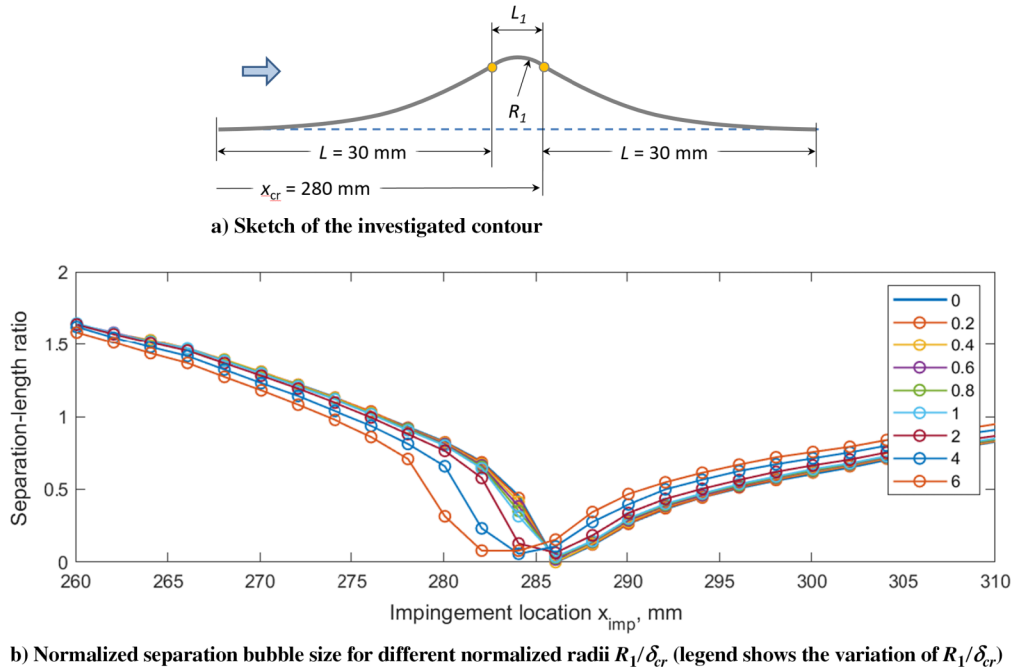
a) Sketch of the investigated contour

b) Normalized separation bubble size for different normalized radii R_1/δ_{cr} (legend shows the variation of R_1/δ_{cr})

Fig. 17   Effect of bump-crest rounding at different x_{imp} at $M_1 = 3.0$ and $\beta = 12$ deg.

than the total length of the applied concave bump. In a targeted application, the bump extension should definitely exceed the length of the initial separation bubble to be maximally effective. Thus, it is not a fundamental problem of the considered solution but an important hint for the adjustment of the geometry, which might be necessary at low Mach numbers. The influence of the design length of the bump on its effectiveness was not further investigated in this study.

IV.   Conclusions

In the present work the potential of a novel device, a shock-canceling concave bump, for control of flow separation and reduction of total-pressure losses induced by a 2-D impinging shock/boundary-layer interaction was investigated numerically. The resulting findings were supported by experimental results. The investigations were performed at freestream Mach numbers M_1 ranging from 2.5 to 5.0 for shock-generator angles β varying from 6 to 12 degrees. The most important results of this study can be summarized as follows:

1) A simplified method for preliminary design of concave bumps based on a generalized representation of the shock-canceling bump shape has been proposed and demonstrated. The method helps to adjust the wall contour in the region of any incident 2-D shock wave so that the formation of the separation bubble is avoided/suppressed.

2) The analytical study has shown that a shock-canceling concave-bump contour can be described by simple relations using the total length and the maximum deflection angle of the bump as design parameter.

3) The numerical study has shown that the application of the concave bump can practically suppress the separation of the flow even for the strongest interaction case analyzed in this study ($M_1 = 2.5$, $\beta = 12$ deg) compared to the baseline situation without bump. At optimal conditions, a reduction in momentum thickness of up to 31% and an increase in mean total pressure recovery of up to 33% were observed in the near-wall flow downstream of the interaction zone. For maximum effect, the bump length should be comparable to or exceed the separation bubble length expected in the reference case.

4) The influence of the displacement thickness on the effective flow-deflection angle along the bump leads in reality to a delayed increase of the wall pressure compared to the simplified prediction. As a result, the pressure distribution in a viscous flow is always flatter on the wind side and always steeper on the lee side than assumed in a nonviscous flow. Increasing the inflow Mach number leads to a significant amplification of this effect due to the increase in compressibility of the flow.

5) The results show that the concave bump is less effective when the incident shock wave does not optimally strike the bump crest. It is particularly unfavorable if the actual shock impingement location is on the windward side of the bump. However, this effect is less pronounced when the shock impact occurs on the leeward side (downstream of the expansion kink). Particularly in the strongest interaction cases, the induced positive effect is maintained practically in the entire leeward area of the bump.

6) The investigations into the effect of a rounded bump edge instead of the ideally sharp-edged contour have shown that the maximum achievable gains are almost retained even if radii are increased, but only decrease slightly. If the normalized radius R_1/δ_{cr} of the rounded region is increased from 0 to 6 in the documented case $M_1 = 3$, $\beta = 12$ deg, the separation length could still be reduced by up to 90%. Thus, the rounding of the edge could be a viable option for a concrete realization of the device.

Most of the quantitative results presented here are based on numerical simulations. Although these have been carried out very carefully and the current results for the reference SWBLI flow were validated with experimental datasets known from the literature, they require a final experimental verification.

References

[1] Goldberg, T. J., and Hefner, J. N., "Starting Phenomena for Hypersonic Inlets with Thick Turbulent Boundary Layers at Mach 6," NASA TN D-6280, 1971.

[2] Van Wie, D. M., Kwok, F. T., and Walsh, R. F., "Starting Characteristics of Supersonic Inlets," AIAA Paper 1996-2914, 1996.

[3] Van Wie, D. M., "Scramjet Inlets," *Scramjet Propulsion*, edited by E. T. Curran, and S. N. B. Murthy, Progress in Astronautics and Aeronautics, Vol. 189, AIAA, Reston, VA, 2001, pp. 447–511.

[4] Syberg, J., and Koncsek, J. L., "Bleed System Design Technology for Supersonic Inlets," *Journal of Aircraft*, Vol. 10, No. 7, 1973, pp. 407–413.
https://doi.org/10.2514/3.60241

[5] Slater, J., "CFD Methods for Computing the Performance of Supersonic Inlets," AIAA Paper 2004-3404, 2004.

[6] Liepmann, H. W., and Roshko, A., Elements of Gasdynamics, Galcit Aeronautical Series, Wiley Inc., New York, 1957, p. 116.

[7] Zhang, Y., Tan, H.-J., Zhuang, Y., and Wang, D.-P., "Influence of Expansion Waves on Cowl Shock/Boundary Layer Interaction in Hypersonic Inlets," *Journal of Propulsion and Power*, Vol. 30, No. 5, 2014, pp. 1183–1191.
https://doi.org/10.2514/1.B35090

[8] Zhang, Y., Tan, H.-J., Li, J.-F., and Yin, N., "Control of Cowl-Shock/Boundary-Layer Interactions by Deformable Shape-Memory Alloy

Bump," *AIAA Journal*, Vol. 57, No. 2, 2019, pp. 696–705.
https://doi.org/10.2514/1.J057409

[9] Pearcey, H. H., "Shock Induced Separation and its Prevention by Design and Boundary Layer Control," *Boundary Layer and Flow Control*, edited by G. V. Lachmann, Progress in Astronautics and Aeronautics, Vol. 2, Pergamon, New York, 1961, pp. 1277–1312.

[10] Stanewsky, E., Delery, J., Fulker, J. L., and Geißler, W. (eds.), *EUROSHOCK—Drag Reduction by Passive Shock Control*, Vol. 56, Notes on Numerical Fluid Mechanics, Springer-Verlag, Berlin, 1997, pp. 85–414.

[11] Ashill, P. R., and Fulker, J. L., "A review of Flow Control Research at DERA," *Proceeding of IUTAM Symposium on Mechanics of Passive and Active Flow Control*, edited by G. E. A. Meier, and P. R. Viswanath, Kluwer Academic, Norwell, MA, 1999, pp. 43–56.

[12] Stanewsky, E., Delery, J. L., Fulker, J., and Matteis, P. (eds.), *Drag Reduction by Shock and Boundary Layer Control*, Vol. 80, Notes on Numerical Fluid Mechanics and Multidisciplinary Design, Springer-Verlag, Berlin, 2002, pp. 359–431.
https://doi.org/10.1007/978-3-540-45856-2

[13] Babinsky, H., and Harvey, J. K. (eds.), *Shock Wave-Boundary-Layer Interactions*, Cambridge Aerospace Series, Cambridge Univ. Press, Cambridge, England, U.K., 2011, pp. 5–86.
https://doi.org/10.1017/CBO9780511842757

[14] Holden, H. A., and Babinsky, H., "Separated Shock-Boundary-Layer Interaction Control Using Streamwise Slots," *Journal of Aircraft*, Vol. 42, No. 1, 2005, pp. 166–171.
https://doi.org/10.2514/1.4687

[15] Shinde, V. J., Gaitonde, D. V., and McNamara, J. J., "Control of Transitional Shock Wave Boundary Layer Interaction Using Surface Morphing," AIAA Paper 2019-1895, Jan. 2019.
https://doi.org/10.2514/6.2019-1895

[16] Shinde, V. J., Gaitonde, D. V., and McNamara, J. J., "Supersonic Turbulent Boundary-Layer Separation Control Using a Morphing Surface," *AIAA Journal*, Vol. 59, No. 3, 2021, pp. 912–926.
https://doi.org/10.2514/1.J059773

[17] Gaitonde, D. V., "Progress in Shock Wave/Boundary Layer Interactions," *Progress in Aerospace Sciences*, Vol. 72, Jan. 2015, pp. 80–99.
https://doi.org/10.1016/j.paerosci.2014.09.002

[18] Souverein, L. J., Bakker, P. G., and Dupont, P., "A Scaling Analysis for Turbulent Shock-Wave/Boundary-Layer Interactions," *Journal of Fluid Mechanics*, Vol. 714, Jan. 2013, pp. 505–535.
https://doi.org/10.1017/jfm.2012.495

[19] Touré, P. S. R., and Schülein, E., "Scaling for Steady and Traveling Shock Wave/Turbulent Boundary Layer Interactions," *Experiments in Fluids*, Vol. 61, No. 156, 2020, pp. 1–19.
https://doi.org/10.1007/s00348-020-02989-5

[20] Schwamborn, D., Gerhold, T., and Heinrich, R., "The DLR TAU-Code: Recent Applications in Research and Industry," *ECCOMAS CFD 2006: Proceedings of the European Conference on Computational Fluid Dynamics*, edited by P. Wesseling, E. Oñate, and J. Périaux, TU Delft, Delft, The Netherlands, 2006, p. 1–25.

[21] Schülein, E., "Supersonic Inlet with a Contour Bump/"Berschalleinlauf mit Einer Konturbeule," German Aerospace Center DLR, DE Patent application, DE 10 2020 117 768 A1, 06.07.2020, 2020.

[22] Touré, P. S. R., and Schülein, E., "Numerical and Experimental Study of Nominal 2-D Shock-Wave/Turbulent Boundary Layer Interactions," AIAA Paper 2018-3395, June 2018.
https://doi.org/10.2514/6.2018-3395

[23] Brown, J. L., "Shock Wave Impingement on Boundary Layers at Hypersonic Speeds: Computational Analysis and Uncertainty," AIAA Paper 2011-3143, June 2011.
https://doi.org/10.2514/6.2011-3143

[24] Settles, G. S., *Schlieren and Shadowgraph Techniques: Visualizing Phenomena in Transparent Media, Experimental Fluid Mechanics*, Springer-Verlag, Berlin, 2001, p. 29.
https://doi.org/10.1007/978-3-642-56640-0

F. Grasso
Associate Editor